Morphologically constrained modeling of spinous inhibition in the somato-sensory cortex

Olivier Gemin[1,†], Pablo Serna[1,2,†], Nora Assendorp[1], Matteo Fossati[1,3,4], Philippe Rostaing[1], Antoine Triller[1*] and Cécile Charrier[1*]

[1] Institut de Biologie de l'Ecole normale supérieure (IBENS), CNRS, INSERM, PSL Research University, 75005 Paris, France

[2] Laboratoire de Physique de l'Ecole Normale Supérieure, ENS, PSL Research University, CNRS, Sorbonne Université, Université Paris-Diderot, Sorbonne Paris Cité, Paris, France 75005

[3] Present adress: CNR – Institute of Neuroscience, via Manzoni 56, 20089 Rozzano (MI), Italy

[4] Present adress: Humanitas Clinical and Research Center - IRCCS -, via Manzoni 56 20089, Rozzano (MI), Italy

[†]: Contributed equally to this work

*: Corresponding authors

Correspondence to: antoine.triller@ens.psl.eu and cecile.charrier@ens.psl.eu

ABSTRACT

Pyramidal neurons are covered by thousands of dendritic spines receiving excitatory synaptic inputs. The ultrastructure of dendritic spines shapes signal compartmentalization but ultrastructural diversity is rarely taken into account in computational models of synaptic integration. Here, we developed a 3D correlative light-electron microscopy (3D-CLEM) approach allowing the analysis of specific populations of synapses in genetically defined neuronal types in intact brain circuits. We used it to reconstruct segments of basal dendrites of layer 2/3 pyramidal neurons of adult mouse somatosensory cortex and quantify spine ultrastructural diversity. We found that 10% of spines were dually-innervated and 38% of inhibitory synapses localize to spines. Using our morphometric data to constrain a model of synaptic signal compartmentalization, we assessed the impact of spinous versus dendritic shaft inhibition. Our results indicate that spinous inhibition is locally more efficient than shaft inhibition and that it can decouple voltage and calcium signaling, potentially impacting synaptic plasticity.

INTRODUCTION

In the mammalian cortex, the vast majority of excitatory synapses are formed on dendritic spines, small membrane protrusions that decorate the dendrites of pyramidal neurons (PNs) (Ramon y Cajal, 1899; Hersch and White, 1981; Yuste and Bonhoeffer 2004). Dendritic spines are composed of a bulbous head connected to the dendritic shaft by a narrow neck (Arellano, 2007; Harris and Weinberg, 2012). They exist in a large variety of shapes and sizes along individual dendrites. Spine head volume can vary between 3 orders of magnitude (0.01-1.5 μm^3), neck length between 0.2 µm and 3 µm, and minimal neck diameter between 20 and 500 nm (Harris et al., 2015). Spine heads are typically contacted by an excitatory synaptic input and harbor an excitatory post-synaptic density (ePSD) that contains glutamatergic α-amino-3-hydroxy-5-methyl-4-isoxazolepropionic acid (AMPA) and N-Methyl-D-aspartate (NMDA) neurotransmitter receptors, scaffolding proteins, adhesion molecules and a complex machinery of proteins undertaking the transduction of synaptic signals. The size of the spine head correlates with the size of the ePSD and the strength of synaptic transmission (Fifková and Anderson, 1981; Nusser et al., 1997; Matsuzaki et al., 2004; Bourne and Harris, 2011; Holderith et al., 2012). In addition to the ePSD, spines contain ribosomes, which mediate local protein synthesis, and endosomes, which play a critical role in membrane and receptor trafficking (Bailey et al., 2015; Kennedy and Hanus, 2019). The largest spines often contain a spine apparatus (SA), which contributes to calcium signaling and synaptic plasticity (Korkotian et al., 2014; Bailey et al., 2015), and some spines, especially in the upper layers of the cortex,

are also contacted by an inhibitory synaptic input (dually-innervated spines or DiSs; Kubota et al., 2007). Spine necks are diffusional barriers that biochemically isolate spine heads from their parent dendrite (Alvarez and Sabatini, 2007; Tønnesen et al., 2014; Adrian et al., 2017; Yasuda, 2017). In addition, they can filter the electrical component of synaptic signals and amplify spine head depolarization (Harnett et al., 2012; Yuste, 2013; Tønnesen and Nägerl, 2016; but see Svoboda et al., 1996; Takasaki and Sabatini, 2014; Popovic et al., 2015). Both spine heads and spine necks are remodeled depending on neuronal activity (Matsuzaki et al., 2004; Honkura et al., 2008, Araya et al., 2014) and in pathology (Androuin et al., 2018; Forrest et al., 2018). While widely acknowledged, the extent of synaptic ultrastructural diversity along individual dendrites has not been quantified, and the consequences of this variability on signal compartmentalization and dendritic integration remain to be investigated.

Dendritic signaling can be modeled based on anatomical and biophysical parameters (Poirazi and Papoutsi, 2020) using “realistic” multi-compartment models (Almog and Korngreen, 2016). These models were pioneered by Wilfrid Rall following the seminal works of Hodgkin and Huxley (Rall, 1970; Hodgkin and Huxley, 1952). They have provided a powerful theoretical framework for understanding dendritic integration (Stuart and Spruston, 2015), spine function (Segev and Rall, 1988), inhibitory signaling (Gidon and Segev, 2012; Doron et al., 2017) and electrical compartmentalization in spines (Yuste et al., 2000, Gulledge et al., 2012; Tønnesen and Nägerl, 2016). However, spines and synapses are usually modeled with *ad hoc* averaged biophysical parameters, which limits prediction accuracy. Modeling the actual behavior of dendritic spines requires an accurate description of their ultrastructural heterogeneity along identified dendrites of specific types of neurons. To acquire such data, it is necessary to combine the nanometer resolution of electron microscopy (EM) with an approach that allows the identification of the origin of dendritic spines (i.e. location on the dendrite, type of dendrite and type of neuron) without obscuring the intracellular content. This task is arduous: 1 mm^3 of mouse cortex contains over 50,000 of neurons, each of which establishes approximately 8,000 synaptic connections with neighboring neurons, and these synapses are highly specific, connecting multiple neuronal subtypes from various brain regions (Schüz and Palm, 1989; Herculano-Houzel et al., 2013; Motta et al., 2019; Sanes and Zipursky, 2020). Reconstructing selected dendritic spines and synaptic contacts along dendritic trees requires either: enormous volumes of 3D-EM acquisitions using resource-consuming approaches adapted from connectomics (Briggman and Denk, 2006; Helmstaedter, 2013; Kasthuri et al., 2015; Karimi et al., 2020), or combining EM with a lower-scale imaging modality, such as confocal or 2-photon light microscopy (LM), to guide 3D-EM image acquisitions to the region of interest (ROI) (De Boer et al., 2015; Begemann and Galic, 2016; Müller-Reichert and Verkade, 2017). While very powerful *in vitro* (Watanabe et al., 2011; Russell et al., 2017, de Boer et al., 2015), correlative light-electron microscopy (CLEM) is

difficult to implement in brain tissues (Collman et al., 2015; Lees et al., 2017; Maclachlan et al., 2018). New protocols are required to facilitate the identification of targeted dendrites and synapses in 3D-EM.

Here, we have developed a CLEM workflow combining confocal light microscopy with serial block-face scanning EM (SBEM) and targeted photo-precipitation of 3,3-diaminobenzidine (DAB) to facilitate ROI recovery. We applied this workflow to reconstruct dendritic spines located exclusively on the basal dendrites of genetically-labelled PNs in layers 2/3 of the somatosensory cortex (SSC) of adult mice. We analyzed the variability of their ultrastructure and estimated the electrical resistance of their neck. We also examined the distribution and the morphology of inhibitory synapses. We specifically examined dendritic spines receiving both excitatory and inhibitory inputs, which represented 10% of all spines along basal dendrites. These dually-innervated spines (DiSs) exhibited wider heads and larger ePSDs than singly-innervated spines (SiSs), and they were more electrically isolated from the dendritic shaft than SiSs of comparable head size. We then used our measurements to constrain a multi-compartment model of synaptic signaling and compartmentalization in dendrites. We assessed the effects of individual excitatory and inhibitory signals on membrane voltage and calcium concentration depending on inhibitory synapse placement (i.e. on a spine head or on the dendritic shaft) and input timing. Our results challenge the view that spinous inhibition strictly vetoes single excitatory inputs and rather suggest that it fine-tunes calcium levels in DiSs. Our simulations indicate that a single inhibitory postsynaptic potential (IPSP) evoked in a DiS within 10 ms after an excitatory postsynaptic potential (EPSP) can curtail the local increase of calcium concentration without affecting the amplitude of membrane depolarization. This decoupling effect could impact long-term synaptic plasticity in cortical circuits.

RESULTS

Combining light and electron microscopy to access the ultrastructure of targeted populations of dendritic spines in brain slices

In the cortex, the morphology and distribution of dendritic spines vary depending on cortical area and layer in which the cell body is located (Katz et al., 2009; Harris and Weinberg, 2012; Bosch et al., 2015; Stuart and Spruston, 2015), and dendritic spines are differently regulated depending on their location within dendritic trees — e.g. basal or apical dendrites (Globus et al., 1973; Feldmeyer et al., 2012; Bian et al., 2015; Rajkovich et al., 2017; Karimi et al., 2020). Therefore, it is critical to take into account both the cellular and dendritic context to characterize the diversity of spine ultrastructure. To that aim, we developed a 3D-CLEM workflow allowing the ultrastructural characterization of dendritic spines on genetically-defined

128 neuronal cell types and along identified types of dendrites in intact cortical circuits. In order to
129 label specific subtypes of neurons, we used cortex-directed *in utero* electroporation (IUE) in
130 mice. We electroporated neuronal progenitors generating layer 2/3 cortical PNs at embryonic
131 day (E)15.5 with a plasmid expressing the fluorescent cytosolic filler tdTomato, granting
132 access to the morphology of electroporated neurons, their dendrites and their dendritic spines
133 in LM. We perfused adult mice with aldehyde fixatives, and collected vibratome sections of
134 the electroporated area. To facilitate sample handling, we designed custom-made chambers
135 allowing sample immersion in different solutions during confocal imaging and subsequent
136 retrieval of the sample before EM preparation steps (Supplementary figure 1A). We enclosed
137 10-20 mm^2 fragments of brain sections in these chambers and acquired images of optically
138 isolated basal dendrites of bright electroporated neurons with confocal microscopy (Figure
139 1A).

140 A major challenge of CLEM in brain tissue is to recover the ROI in EM after imaging in
141 LM. Several methods have been proposed to facilitate ROI recovery (De Boer et al., 2015;
142 Begemann and Galic, 2016; Müller-Reichert and Verkade, 2017), but they come with caveats:
143 (1) using only intrinsic landmarks has a low throughput (Luckner et al., 2018; Maclachlan et
144 al., 2018); (2) filling target neurons with 3,3-diaminobenzidine (DAB) masks intracellular
145 ultrastructure (Meißlitzer-Ruppitsch et al., 2009); (3) scarring the tissue with an infra-red laser
146 to generate extrinsic landmarks, a.k.a. "NIRB", for "near-infrared branding" (Bishop et al.,
147 2011; Maco et al., 2013; Cane et al., 2014; Blazquez-Llorca et al., 2015; Lees et al., 2017),
148 produces landmarks with low pixel intensity in EM and can damage ultrastructure (Karreman
149 et al., 2016; Luckner et al., 2018). To facilitate ultrastructural measurements in non-obscured
150 identified dendrites, we took advantage of the photo-oxidability of DAB (Lübke, 1993;
151 Grabenbauer et al., 2005). We immersed the samples in DAB solution and applied focalized
152 UV light at user-defined positions (Figure 1A) to imprint osmiophilic DAB landmarks around
153 targeted dendrites (Supplementary figure 1B-E) and pattern the tissue with localized electron-
154 dense DAB precipitates (Figure 1B). After sample retrieval (Supplementary figure 1F), tissue
155 sections were processed for SBEM and embedded in minimal amounts of epoxy resin in order
156 to maximize sample conductivity and SBEM image quality (see Methods). In 3D-EM stacks,
157 ROIs were recovered within the complex environment of brain tissues using both intrinsic
158 landmarks such as blood vessels (Figure 1B), and high-contrast DAB precipitates (Figure 1C;
159 see also supplementary figure 1G). We then segmented and reconstructed targeted dendrites
160 in 3D, and registered whole dendritic portions in both LM and EM to identify each dendritic
161 spine unequivocally using neighboring spines as dependable topographic landmarks (Figure
162 1D). CLEM-based 3D-reconstruction enabled the identification of dendritic spines that were
163 not visible in LM or EM alone. In LM, the limited axial resolution prevents the identification of
164 axially oriented spines, which are easily detected in 3D-EM (Karimi et al., 2020) (Figure 1D).

165 On the other hand, spines with the longest and thinnest necks are conspicuous in LM stacks,
166 but can be difficult to find in 3D-EM datasets without the cues provided by LM. The proportion
167 of spines recovered with CLEM versus LM alone could amount to up to 30% per ROI, and 5%
168 per ROI versus EM alone, highlighting the advantage of CLEM over unimodal microscopy
169 approaches.
170
171 **Spine ultrastructure along the basal dendrites of L2/3 cortical pyramidal neurons.**
172 We used our CLEM workflow to quantify the full extent of the ultrastructural diversity of
173 dendritic spines along the basal dendrites of layer 2/3 PNs of the SSC of three adult mice. We
174 exhaustively segmented 254 µm of the basal dendritic arborization of four neurons and we
175 reconstructed a total of 390 individual spines (Supplementary table 1). As spine distance to
176 the soma spanned from 20 to 140 µm, with basal dendrites extending up to 150 µm
177 (Ballesteros-Yañez et al., 2006; Chen et al., 2012; Sarid et al., 2015; Kubota et al., 2015), we
178 consider that our dataset is representative of the whole spine population on these dendrites.
179 The average linear density of dendritic spines was 1.5 ± 0.3 spine.μm^{-1}. We then quantified
180 the following parameters for each spine: neck length, neck diameter, head volume, head
181 longitudinal diameter (referred to as “head length”), head orthogonal diameter (referred to as
182 “head diameter”), number of PSDs, and PSD area (Figure 2A; Supplementary table 2). In
183 agreement with previous reports in both basal and apical dendrites of mouse cortical and
184 hippocampal neurons (Knott et al., 2006; Arellano, 2007; Noguchi et al., 2011; Harris et al.,
185 2014), we found that ePSD area correlates linearly with the volume of the spine head (Figure
186 2B). We also observed a non-linear correlation between the length of the spine neck and its
187 diameter (Figure 2C): long spines (neck length > 2 µm) always had thin necks (neck diameter
188 < 0.2 µm), although short necks could also be thin. Furthermore, in spines with long necks,
189 spine heads were always stretched longitudinally with respect to the neck (i.e. prolate)
190 whereas they could also be stretched orthogonally (i.e. oblate) in shorter spines (Figure 2D),
191 with a possible impact on nanoscale ion flows (Bell et al., 2019; Lagache et al., 2019). By
192 contrast, there was no correlation between the position of the spine or between the inter-spine
193 distance and any of the morphological parameters we measured (data not shown), in line with
194 previous ultrastructural studies (Arellano, 2007). There was also no correlation between the
195 length or the diameter of the neck and the morphometry of the spine head or ePSD, which is
196 consistent with previous EM studies of L2/3 PNs of mouse neocortex (Arellano, 2007;
197 Ballesteros-Yáñez et al. 2006; but see Gulledge et al., 2012, and Noguchi et al., 2005 for
198 different conclusions in other brain areas).
199 Since our CLEM approach grants access to the cytosolic content of spines (Figure 3A),
200 we quantified the occurrence of SA, a complex stacked-membrane specialization of smooth
201 endoplasmic reticulum (SER) which contributes to calcium signaling, integral membrane

202 protein trafficking, local protein synthesis, and synaptic plasticity (Bourne and Harris, 2008;
203 Segal and Korkotian, 2014; Korkotian et al., 2014; Bailey et al., 2015; Kennedy and Hanus,
204 2019). In basal dendrites, about 54% of spines contained a SA (Figure 3B), which is
205 substantially higher than previous reports in the mature hippocampus (Bailey et al., 2015;
206 Chirillo et al., 2019). These spines were randomly distributed along the dendrites. They had
207 larger heads (Figure 3C), larger ePSDs (Figure 3D) and wider necks than spines devoid of
208 SA (Figure 3E), consistent with previous morphological studies of CA1 PNs (Bailey et al.,
209 2015; Spacek and Harris, 1997; Chirillo et al., 2019). The probability that a spine contained a
210 SA depending on spine head volume followed a sigmoid model (Figure 3F), predicting that all
211 spines with a head diameter larger than 1.1 µm (21% spines in our reconstructions) contain a
212 SA. Interestingly, SER was also often detected at the stem of half of spines devoid of SA (25%
213 of all spines), but these spines did not differ in their morphology from other spines devoid of
214 SA (data not shown).
215 Next, we used our ultrastructural data to estimate the electrical resistance of spine
216 necks using $R_{neck} = \rho W_{neck}$, where ρ is the cytosolic resistivity (set to 300 Ω.cm; Elbohouty et
217 al., 2013; Miceli et al., 2017) and W_{neck} is the diffusional neck resistance that restricts the
218 diffusion of molecules and charges between spine heads and dendritic shafts (Svoboda et al.,
219 1996). To quantify W_{neck}, for each spine we measured a series of orthogonal cross-sections
220 of the neck along its principal axis and integrated $W_{neck} = \int dl/A(l)$, where A(l) is the neck
221 cross-section area at the abscissa l along the neck axis. W_{neck} ranged from 2 μm^{-1} to 480 μm^{-1}
222 and R_{neck} from 8 MΩ to 1450 MΩ, with a median value of 188MΩ. These values are consistent
223 with previous estimations based on EM reconstructions and STED super-resolutive light
224 microscopy (Harris and Stevens, 1989; Tønnesen et al., 2014), and with direct
225 electrophysiological recordings (Jayant et al, 2017). It has been proposed that spine
226 apparatuses, which occupy some of the spine neck volume, could increase W_{neck} (Bourne and
227 Harris, 2008; Lagache et al., 2019; Kennedy and Hanus, 2019). Therefore, we subtracted SA
228 cross-section from A(l) when computing W_{neck} in SA+ spines (see Methods). This correction
229 increased W_{neck} by 13% ± 2% in SA+ spines (Supplementary figure 2). However, because of
230 their wider necks, W_{neck} of SA+ spines was still lower (59% in average) than W_{neck} of spines
231 devoid of SA (Figure 3G). These results suggest that, in addition to supplying large dendritic
232 spines with essential resources, the SA may adjust W_{neck} and influence spine
233 compartmentalization (Bailey et al., 2015; Chirillo et al., 2019; Kennedy and Hanus, 2019).
234
235 **Excitatory and inhibitory synapses in dually-innervated spines.**
236 We noticed that a significant proportion of dendritic spines were contacted by two distinct pre-
237 synaptic boutons (DiSs). DiSs have long been described in the literature as receiving both an
238 excitatory and an inhibitory synaptic contact (Jones and Powell, 1969; Beaulieu and Colonnier,

239 1985; Dehay et al., 1991; Fifková et al., 1992). In the somato-sensory cortex, DiSs are
240 contacted by VGLUT2-positive thalamocortical inputs (Kubota et al., 2007) and they are
241 sensitive to sensory experiences. The number of DiSs increases in response to sensory
242 stimulation and decreases in response to sensory deprivation (Micheva and Beaulieu, 1995;
243 Knott et al., 2002; Chen et al., 2012; van Versendaal et al., 2012), suggesting their importance
244 in synaptic integration and sensory processing. While ePSDs look asymmetrical and more
245 electron-dense than inhibitory PSDs (iPSDs) in transmission EM (Gray, 1959; Uchizono,
246 1965), the anisotropic resolution of SBEM does not allow the distinction of ePSDs and iPSDs
247 in most DiSs (Karimi et al., 2020). Therefore, to label inhibitory synapses in cortical PNs
248 (Figure 4A), we co-expressed tdTomato with small amounts of GFP-tagged gephyrin (GFP-
249 GPHN) (Chen et al., 2012; van Versendaal et al., 2012; Fossati et al., 2016; Iascone et al.,
250 2020), a core component of inhibitory postsynaptic scaffolds (Tyagarajan and Fritschy, 2014;
251 Krueger-Burg et al., 2017). We identified in LM spines containing a gephyrin cluster (Figure
252 4B) and we ascertained their dual-innervation in EM after back-correlating spine identity
253 between LM and SBEM acquisitions. To do so, we aligned reconstructed dendrites on LM
254 images (Figure 4C), and matched individual spines in both modalities (lettered in Figures 4B
255 and 4C). We identified iPSDs on DiSs based on GFP-GPHN cluster position in LM images. In
256 89% of DiSs (33/37), the excitatory (GFP-GPHN-negative) PSD and the inhibitory (GFP-
257 GPHN-positive) PSD could be clearly discriminated. However, in 11% of DiSs (4/37 DiSs),
258 distinguishing ePSD from iPSD was not obvious due to the coarse axial resolution of LM
259 imaging. To resolve ambiguities, we reconstructed the axons innervating the DiSs and
260 determined their identity based on their other targets in the neuropil, either soma and dendritic
261 shaft for inhibitory axons (Hersch and White, 1981; Isaacson and Scanziani, 2011; Boivin and
262 Nedivi, 2018), or other dendritic spines for excitatory axons (Karimi et al., 2020) (Figure 4D).
263 As a result, we could unequivocally determine the excitatory or inhibitory nature of each
264 synaptic contact on electroporated neurons, within ~10^5 μm^3 3D-EM acquisition volume.
265 In CLEM, we measured an average density of 1.4 ± 0.5 iPSDs per 10 µm of dendrite
266 on DiSs and 2.1 ± 1.2 iPSDs per 10 µm of dendrite on the dendritic shaft— amounting to 3.5
267 ± 1.1 iPSDs per 10 µm of dendrite. We observed a homogeneous distribution of iPSDs located
268 either on spines or shaft, from 24 µm away from the soma to the dendritic tip, in contrast to
269 apical dendrites where spinous inhibitory synapses are distally enriched (Chen et al., 2012).
270 Along the basal dendrites of L2/3 cortical PNs, 38% of inhibitory contacts occurred in dendritic
271 spines, which is in the range of, or slightly higher than previously estimated using LM only
272 (Chen et al., 2012; Iascone et al., 2020). DiSs represented 10% ± 3% of all spines (Figure
273 5A). They had larger heads than SiSs (Figure 5B), in line with previous reports (Kubota et al.,
274 2007; Villa et al., 2016), and 86% ± 13% of them contained a SA (Figure 5C). DiSs also differed
275 in terms of neck morphology. They had longer necks than SiSs of comparable head volume

(V_{head} >0.05 μm^3), although neck length distribution was similar in the whole populations of SiSs and DiSs (Figure 5D). DiSs also had lower D_{neck}/V_{head} ratio than SiSs (Figure 5E), although D_{neck} distribution was similar between SiSs and DiSs (Supplementary figure 3), suggesting that excitatory signals generated in DiSs are more compartmentalized than signals of similar amplitude generated in SiSs. Accordingly, DiSs had a higher W_{neck} than SiSs of comparable head size (52% larger in average) (Figure 5F). In spine heads, ePSDs on DiSs were larger than ePSDs on SiSs (174% ± 113% of ePSD area) (Figure 5G), consistent with the larger head size of DiSs. By contrast, iPSDs on DiSs were smaller than shaft iPSDs (53% ± 15% of shaft iPSD area) (Figure 5H), in line with previous reports in rat L5 PNs (Kubota et al., 2015). The area of iPSDs on DiSs did not correlate with spine head volume (data not shown). In 95% of DiSs, iPSDs were smaller than ePSDs (half the area, in average) (Figure 5I). Together, these results indicate that DiSs represent a specific population of dendritic spines with distinctive ultrastructural features that could impact their functional properties.

Morphologically constrained model of synaptic signaling

Next, we wanted to assess the impact of spine diversity on synaptic signals. We used a computational approach based on a multi-compartment “ball-and-stick” model of the neuronal membrane (Rall, 1964; Gulledge et al., 2012). This model comprises an isopotential soma and two dendritic compartments structured as cables featuring passive resistor-capacitor (RC) circuits and conductance-based synapses. The two dendritic compartments correspond to the dendrite receiving the synaptic inputs and to the remainder of the dendritic tree (Figure 6A1) (Dayan and Abbot, 2001; Stuart et al., 2016). We constrained this model with morphological parameters measured in CLEM (i.e. distance between spine and soma, neck resistance, head volume, head membrane area, ePSD area and iPSD area for 390 spines, and dendritic diameter), taking into account the structural shrinkage resulting from chemical fixation (Supplementary figure 4). Excitatory and inhibitory synaptic conductances were modeled as bi-exponential functions of time, with their rise and decay times tuned to the kinetics of different receptor types: AMPA and NMDA receptors at ePSDs, and type A γ-aminobutyric acid ($GABA_A$) receptors at iPSDs (Figure 6A2; see Methods). Individual synaptic conductances were scaled proportionally to PSD areas (Nusser et al., 1998; Matsuzaki et al., 2004; Noguchi et al., 2011). Voltage-dependent calcium channels (VDCCs) in spine heads were modeled using Goldman–Hodgkin–Katz equations (Koch and Segev, 1998) and their conductance was scaled proportionally to spine head areas.

We adjusted excitatory synaptic conductivity so that average amplitudes of both synaptic currents and somatic depolarizations evoked by individual excitatory post-synaptic potentials (EPSPs) fitted published electrophysiological values (Feldmeyer et al., 2006, Frik et al., 2008, Lefort et al., 2009, Scala et al., 2018) (see Methods). After calibration of excitatory

synapses, maximal synaptic conductance ranged from 0.04 nS to 3.13 nS for g_{AMPA} (0.456 ± 0.434 nS) and from 0.04 nS to 3.42 nS for g_{NMDA} (0.498 ± 0.474 nS), in line with the literature (Hoffmann et al., 2015). We then adjusted inhibitory synaptic conductivity to set the mean conductance of dendritic inhibitory synapses to 1 nS (Gidon and Segev, 2012; Xu et al., 2013; Kobayashi et al., 2008). As a result, g_{GABA} ranged from 0.33 nS to 3.36 nS (1.00 ± 0.577 nS) for synapses located on the shaft, and from 0.19 nS to 1.56 nS (0.528 ± 0.277 nS) for inhibitory synapses located on spines.

We first examined the propagation of simulated EPSPs. We compared the evoked depolarization amplitude ΔV_{max} in three different compartments: in the spine head in which the EPSP was elicited, in the dendritic shaft close to the spine, and in the soma (Figure 6B). ΔV_{max} followed a log-normal distribution, reflecting the morphological variability of spines (Figure 6B). Due to the passive attenuation of electrical signals along dendritic processes, ΔV_{max} was sharply attenuated between the head of the spine and the dendritic shaft (51% attenuation in average) and about 5% of ΔV_{max} reached the soma (Figure 6B), in line with measurements performed in basal dendrites of L5 cortical PNs using voltage dyes, electrophysiology and glutamate uncaging (Popovic et al., 2015; Acker et al., 2016; see Williams and Stuart, 2003; Nevian et al., 2007; Larkum et al., 2009 for similar measurements in other systems). ΔV_{max} scaled with ePSD area in all compartments (Figure 6C).

To determine the contribution of morphological parameters to the variance of ΔV_{max}, we used a generalized linear model (GLM) (Pedregosa et al., 2011). We analyzed the contribution of the volume, diameter and resistance of spine necks and heads as well as the contribution of ePSD area and distance between spine and soma (L_{dend}) to the amplitude of the signals in the soma and in spine heads. In the soma, ΔV_{max} was mainly determined by A_{ePSD}, which accounted for 89% of its variance when EPSPs were elicited in SiSs (77% when they came from DiSs). The second determinant was L_{dend}, which accounted for 6.4% of the variance of ΔV_{max} for EPSPs generated in SiSs (14.7% in DiSs). The contribution of R_{neck} to the variance of ΔV_{max} in the soma was comparatively negligible (Supplementary table 3), indicating that the passive attenuation of EPSPs along dendrites dominates the contribution of R_{neck} to somatic depolarizations evoked in spines. In the heads of SiSs, A_{ePSD} and R_{neck} accounted for 60% and 19% of the variance of ΔV_{max}, respectively. In the heads of DiSs, the contribution of R_{neck} to ΔV_{max} was much higher, reaching 38% of the variance, while A_{ePSD} contribution dropped to 47% (Supplementary figure 5 and Supplementary table 3). In 56% of dendritic spines, R_{neck} was large enough (>145MΩ) to attenuate EPSP amplitude by >50% across the spine neck, and more than 90% of spine necks attenuated the signal by at least 10% (Figure 6D), suggesting that most spine necks constitutively compartmentalize electrical signals in the head of spines.

349 We also estimated the elevation of calcium ion concentration ($\Delta[Ca^{2+}]$) in spine heads
350 induced by an EPSP. $\Delta[Ca^{2+}]$ was similar in SiSs and DiSs and varied non-linearly with A_{ePSD}
351 (Figure 6E). A_{ePSD} was the main determinant of $\Delta[Ca^{2+}]$, accounting for 30% of the variance in
352 SiSs (45% in DiSs), followed by R_{neck} (9%; Supplementary table 3). As a single EPSP is not
353 sufficient to elicit a Ca^{2+} spike, we did not model Ca^{2+} transients outside of spine heads.
354 Overall, our model provides quantitative insights into the variability of EPSP amplitude
355 originating from spine diversity and highlights differences in the contribution of morphological
356 parameters to spine depolarization and calcium signals in DiSs and SiSs.
357
358 **Spatial interplay of excitatory and inhibitory signals**
359 We used our model to compare the effects of spinous and dendritic shaft inhibition. *In vitro*
360 uncaging experiments have shown that inhibitory contacts located on DiSs could weaken local
361 calcium signals (Chiu et al., 2013), but the consequences on synaptic excitation are still
362 unclear (Kubota et al., 2015; Higley et al., 2014). To understand how spine ultrastructure and
363 iPSD location influence synaptic integration, we modeled the interaction between one IPSP
364 and one EPSP under the constraint of our morphological measurements. Assessing the extent
365 of signal variability originating from spine morphological heterogeneity requires a large number
366 of simulations (N≥1000). Therefore, we used a bootstrapping method (Efron and Tibshirani,
367 1994) (see Methods) to derive N≥1000 sets of parameters from our dataset of 390 spines and
368 62 shaft iPSDs (Supplementary file 1), and provide unbiased estimations of the mean and
369 variance of the signals. Importantly, the strength of inhibition depends on the reversal potential
370 of chloride ions (E_{Cl}-). In healthy mature layer 2/3 cortical PNs, E_{Cl}- typically varies between
371 the resting membrane potential, V_{rest} = -70 mV, and hyperpolarized values (-80 mV) (Doyon
372 et al., 2016). When E_{Cl}- = -70 mV, active inhibitory synapses generate a local increase of
373 membrane conductance, which "shunts" membrane depolarization induced by concomitant
374 EPSPs. When E_{Cl}- < -70 mV, the driving force of Cl^- ions is stronger, GABAergic inputs can
375 hyperpolarize the cell membrane and IPSPs counter EPSPs. These two situations are
376 respectively termed "shunting inhibition" and "hyperpolarizing inhibition" (Gidon and Segev,
377 2012; Doyon et al., 2016).
378 We first assessed the impact of "shunting" IPSPs elicited in the dendritic shaft on
379 individual EPSPs depending on the inter-synaptic distance (Figure 7A). For each iteration of
380 the model (i.e. N=3700 sets of realistic morphological values for spine size, and iPSD location
381 and size), we varied the distance Δx between a spine receiving an EPSP and a shaft iPSD
382 activated simultaneously. For Δx>0, the iPSD was located between the spine and the soma
383 (i.e. "on-path" inhibition, from the viewpoint of the soma), and for Δx<0, the iPSD was located
384 distally to the spine (i.e. "off-path" inhibition). To quantify inhibition, we compared the amplitude

385 of individual EPSPs in the absence ($\Delta V_{max,E}$) or presence ($\Delta V_{max,E+I}$) of inhibition, and
386 computed the drop in voltage $inh_V = 1 - \Delta V_{max,E+I}/\Delta V_{max,E}$. $Inh_V = 0$ indicates that the
387 electrical signal was not affected, $inh_V = 1$ indicates that it was completely inhibited.
388 Importantly, due to the electrical properties of the cell membrane, inh_V depends on where the
389 signal is measured. In the soma, inh_V was maximal (20% in average) when the iPSD was
390 located on-path and it decreased exponentially with Δx when the iPSD was located off-path
391 (exponential decay length: $L_{soma,off}$ = 30 μm) (Figure 7B), highlighting the impact of proximal
392 inhibitory synapses on distal excitatory inputs (Hao et al., 2009; Gidon and Segev, 2012). In
393 the spine where the EPSP was elicited, inh_V decayed exponentially with Δx for both on-path
394 and off-path inhibition (Figure 7C), with respective decay lengths $L_{spine,on}$ = 30 µm and $L_{spine,off}$
395 = 11 µm (also see Supplementary figure 6 for the dependence of decay lengths on the
396 dendritic cross-section). Therefore, shaft inhibition could affect excitatory signals within 40 µm,
397 which corresponds to approximately 50 spines considering the spine density and dendritic
398 diameter that we measured in basal dendrites of L2/3 cortical PN.
399 Next, we focused on DiSs. We modeled N=3700 DiSs and shaft iPSDs (Δx = 0) at
400 random locations on the dendrite, and we compared two configurations per iteration of the
401 model: (1) the ePSD of the DiS and the shaft iPSD were activated simultaneously (Figure
402 8A1); (2) both the ePSD and the iPSD of the DiS were activated simultaneously (Figure 8A2).
403 In the soma, the effect of shaft and spinous inhibition was comparable: inh_V was centered on
404 17%, and reached up to 50% (Figure 8B), in line with somatic recordings following coincident
405 uncaging of glutamate and GABA in acute brain slices (Chiu et al., 2013). By contrast, in the
406 head of all DiSs, spinous inhibition was more efficient than shaft inhibition despite the smaller
407 size of spinous iPSDs compared to shaft iPSDs. Spinous inh_V was centered on 10% and
408 reached up to 35%, whereas dendritic inh_V was centered on 3% and did not reach more than
409 23% (Figure 8C). These results support the notion that the placement of inhibitory synapses
410 structures the detection and integration of excitatory signals (Bono et al., 2017; Boivin and
411 Nedivi, 2018; Chiu et al., 2019), and highlight the role of spinous inhibition in local synaptic
412 signaling.
413 We then run the simulations with a lower chloride reversal potential (E_{Cl^-} = -80 mV) for
414 which GABAergic inputs can hyperpolarize the cell membrane. In numerous simulations, we
415 observed that hyperpolarization could take over depolarization (i.e. inh_V > 1) (Supplementary
416 figure 7A). This was the case in the soma for 37% of simulations, and in the spine where the
417 EPSP was generated for 10% of simulations. With E_{Cl^-} = -80 mV, the median inh_V imposed
418 by spinous inhibition in spine heads was 45%, in line with a previous morphologically
419 constrained model (Kubota et al., 2015) and with the fact that a hyperpolarizing IPSP may
420 block multiple EPSPs depending on iPSD placement (Boivin and Nedivi, 2018). Interestingly,

421 lowering E_{Cl^-} affected spinous and shaft inhibition differently. In the soma, shaft inhibition
422 became more efficient than spinous inhibition (Supplementary figure 7B) due to the larger area
423 of shaft iPSDs. However, in the heads of most DiSs, spinous inhibition remained more efficient
424 than shaft inhibition (Supplementary figure 7C-F). Altogether, our results indicate that spinous
425 inhibition is stronger than shaft inhibition in DiSs, and that their relative weight is modulated
426 by the driving force of chloride ions.
427
428 **Temporal interplay of excitatory and inhibitory signals**
429 Since the efficacy of inhibition depends on the membrane potential at the onset of the IPSP
430 (Koch et al., 1983; Segev and Rall, 1988; Hao et al., 2009; Doron et al., 2017), we addressed
431 the effect of input timing on inhibition efficacy in DiSs. We simulated the interaction of one
432 EPSP and one IPSP generated with a time difference of Δt (Figure 9A). For $\Delta t<0$ (IPSP before
433 EPSP), IPSPs decreased EPSP amplitude (ΔV_{max}) (Figure 9B1). For $\Delta t>0$ (IPSP after EPSP),
434 IPSPs had no effect on ΔV_{max} but abruptly decreased the tail of the EPSPs (Figure 9B2) (Koch
435 et al., 1983). We first compared how spinous and shaft inhibition reduced EPSP duration by
436 comparing the 80-to-20% decay time of the summed signals (τ_{E+I}) to that of uninhibited
437 EPSPs (τ_E). Decay times were minimal at Δt = +4 ms and decreased by 64% and 78% with
438 spinous and shaft inhibition respectively (Figure 9C), which could shorten the integration
439 window of EPSPs and increase the temporal precision of synaptic transmission (Gabernet et
440 al., 2005). The variance of τ_{E+I} was mainly determined by the area of iPSDs (Supplementary
441 table 4). We then quantified how the timing of inhibition affected EPSP amplitude using
442 $inh_V(\Delta t) = 1 - \Delta V_{max,E+I}/\Delta V_{max,E}$. In spine heads, inh_V was an asymmetrical function of Δt
443 (Koch et al., 1983, Segev and Rall, 1988) and it was maximal at Δt = -4 ms for spinous
444 inhibition, and at Δt = -6 ms for dendritic shaft inhibition. Overall, spinous inhibition was
445 stronger than shaft inhibition, decreasing ΔV_{max} by 26.3% and 16.2%, respectively (median
446 values in Figure 9D; see also Supplementary figure 8A for $inh_V(\Delta t)$ with higher E_{Cl^-}).
447 Interestingly, R_{neck} had a negligible contribution to the variance of inh_V in the case of
448 hyperpolarizing inhibition, but a major one (37%) in the case of shunting inhibition
449 (Supplementary table 4), suggesting that spine necks compartmentalize IPSPs differently
450 depending on E_{Cl^-}.
451 Then, we examined the effect of timed inhibition on calcium signaling in spines, using
452 $inh_{[Ca^{2+}]}(\Delta t) = 1 - \Delta[Ca^{2+}]_{max,E+I} / \Delta[Ca^{2+}]_{max,E}$. We observed that $inh_{[Ca^{2+}]}$ peaked at Δt =
453 0 ms for both spinous and shaft inhibition. More precisely, spinous inhibition reduced calcium
454 transient amplitude by 10% in average, reaching >36% in the top 10% simulations, while shaft
455 inhibition reduced it by 8.6% in average and >28% in the top 10% simulations (Figure 9E).
456 These values are in the range of $inh_{[Ca^{2+}]}$ measured with double uncaging experiments (Chiu

457 et al., 2013). Importantly, IPSPs could decrease the amplitude of calcium transients, within a
458 short time-window (Δt between 0 and +10 ms) in which depolarization amplitude was not
459 affected (Figure 9D-E), thereby decoupling calcium signalling from electrical activity in DiSs.
460

461 **DISCUSSION**

462 In the present study, we developed a novel 3D-CLEM workflow allowing the ultrastructural
463 characterization of specific populations of dendritic spines in genetically defined types of
464 neurons. We used this workflow to exhaustively reconstruct spines and synaptic contacts
465 along the basal dendrites of fluorescently labelled L2/3 cortical PNs of the SSC and to provide
466 a quantitative description of their diversity. We input our measurements in a computational
467 model to analyze the variability of electrical and calcium synaptic signals originating from spine
468 ultrastructural diversity, and to characterize the spatio-temporal integration of excitatory and
469 inhibitory inputs. Our results shed light on unique properties of DiSs, which represent 10% of
470 all spines and 38% of all inhibitory synapses along the basal dendrites of L2/3 cortical PNs.
471 We show that while individual inhibitory synapses distributed along dendritic shafts can be
472 powerful enough to block several EPSPs, spinous inhibitory synapses affect excitatory signals
473 more efficiently in DiSs. We also show that the activation of a spinous inhibitory synapse within
474 a few milliseconds after an EPSP can decouple voltage and calcium signals in DiSs, which
475 could impact calcium-dependent signaling cascades that drive spine plasticity.
476 The molecular composition of synapses and their biophysical properties are reportedly
477 heterogeneous along dendrites and across dendritic trees (Yuste et al., 2000; Berglund et al.,
478 2008; Losonczy et al., 2008; Stuart and Spruston, 2015). However, most computational
479 models so far have used *ad hoc* or averaged values as parameters for dendritic spines and
480 excitatory synapses (Sarid et al., 2007; Almog and Korngreen, 2014; Müllner et al., 2015), and
481 considered that all inhibitory synapses were located along the dendritic shaft (Markram et al.,
482 2015). This limits their accuracy (Jadi et al., 2014). Hence, there is a critical need for cell type-
483 and dendritic type-specific measurements of synaptic ultrastructure and placement, and for
484 detailed quantification of synaptic diversity beyond the µm scale in intact brain circuits. The
485 correlative workflow we propose provides a solution to such demand. It is applicable to any
486 type of tissue and allows anatomical measurements of any kind of genetically labelled cells
487 and organelles. One technical limitation is the need for chemical fixation, which may distort
488 tissue morphology (Korogod et al., 2015; Rostaing et al., 2006). Therefore, it may be
489 necessary to correct for tissue shrinkage based on a morphological comparison with physically
490 fixed tissues (Supplementary figure 4B3) in order to reliably depict *in vivo* situations. Future
491 development of aldehyde-free cryo-CLEM methods will be important to grant access to cellular
492 and synaptic ultrastructure in close-to-native environments.

493 Applying 3D-CLEM to the basal dendrites of L2/3 cortical PNs allowed us to
494 quantitatively describe the landscape of synaptic diversity and to characterize the
495 ultrastructural features of a scarce population of dendritic spines receiving both excitatory and
496 inhibitory synaptic inputs (DiSs). In the cortex, DiSs are mostly contacted by VGluT2-positive
497 excitatory thalamo-cortical inputs (Kubota et al., 2007) and they receive inhibition from
498 somatostatin-expressing and parvalbumin-expressing interneurons (Kubota et al., 2016; Chiu
499 et al., 2013), which are the two main sources of inhibitory inputs to the basal dendrites of layer
500 2/3 cortical PNs (Tremblay et al., 2016; Kuljis et al., 2019). *In vivo* 2-photon imaging
501 experiments have shown that DiSs are among the most stable spines along the dendrites of
502 layer 2/3 PNs (Villa et al., 2016). The inhibitory synapse in DiSs is smaller and more labile
503 than inhibitory synapses along dendritic shafts, and it is very sensitive to sensory experience
504 (Knott et al., 2002; Chen et al., 2012; van Versendaal et al., 2012; Villa et al., 2016). Whisker
505 stimulation induces a lasting increase in the occurrence of iPDSs in spines of the barrel cortex
506 (Knott et al., 2002) and monocular deprivation destabilizes iPSDs housed in spines of the
507 visual cortex (Chen et al., 2012; van Versendaal et al., 2012; Villa et al., 2016), suggesting
508 their role in experience-dependent plasticity. Our morphological and computational analysis
509 provides new insights into the biophysical properties of DiSs. We show that DiSs have larger
510 heads and larger ePSDs than SiSs, and most often contain a spine apparatus. However, the
511 ratio between mean spine neck diameter and spine head volume (or ePSD area) was smaller
512 in DiSs than in SiSs, and DiSs had longer necks than SiSs of comparable head volume, so
513 that EPSPs of similar amplitudes encounter a higher neck resistance in DiSs than in SiSs.
514 Thus, DiSs are uniquely compartmentalized by their ultrastructural features and the presence
515 of an inhibitory synapse.
516 Our model predicts that IPSPs occurring in DiSs within milliseconds after an EPSP can
517 curtail calcium transients without affecting depolarization, thereby locally decoupling voltage
518 and calcium signaling. This is expected to impact the induction of long-term forms of synaptic
519 plasticity, such as long-term potentiation (LTP) or long-term depression (LTD), which underlie
520 learning and memory (Bourne and Harris, 2008; Nabavi et al., 2014; Hayashi-Takagi et al.,
521 2015; Segal, 2017). The induction of LTP versus LTD is determined by the magnitude and
522 time course of calcium flux, with brief, high calcium elevation generating LTP, sustained
523 moderate calcium elevation generating LTD, and low calcium level inducing no plasticity
524 (Lisman, 1989; Feldman, 2012; Graupner and Brunel, 2012). Therefore, a small reduction in
525 the amplitude of calcium transients may limit spine potentiation, or even cause depression
526 (Hayama et al., 2013; Higley, 2014; Nakahata and Yasuda, 2018). In the cortex,
527 thalamocortical inputs may contact DiSs on the basal dendrites of L2/3 both directly (excitatory
528 connection) and indirectly through feed-forward inhibition *via* parvalbumin-expressing fast-
529 spiking interneurons (Gabernet et al., 2005; Kimura et al., 2010). The delay between thalamo-

530 cortical excitatory and feed-forward inhibitory signals is typically +1 ms to +3 ms (Gabernet et
531 al., 2005), within the 10 ms time window for voltage-calcium decoupling in DiSs. Therefore,
532 the presence of inhibitory synapses in DiSs could prevent synaptic potentiation and thereby
533 increase the temporal precision of cortical response to sensory stimulation (Knott et al., 2002;
534 Wehr and Zador, 2003; Gabernet et al., 2005). On the contrary, the removal of spine inhibitory
535 synapses could favor synaptic potentiation during experience-dependent plasticity such as
536 monocular deprivation to strengthen inputs from the non-deprived eye (Frenkel et al., 2006;
537 Chen et al., 2012; van Versendaal et al., 2012).
538 Our understanding of synaptic and dendritic computations is intimately linked to the
539 quantitative description of synaptic distribution, ultrastructure, nano-organization, activity and
540 diversity in neural circuits. The CLEM workflow we propose opens new avenues for the
541 ultrastructural characterization of synapses with defined molecular signature characterizing
542 their identity or activation profile in response to certain stimuli or behaviors. Another milestone
543 to better model the biophysics of synaptic integration will be to combine EM and quantitative
544 super-resolution LM to measure the density and nano-organization of molecular species (e.g.
545 AMPARs, NMDARs, voltage-dependent calcium channels) in specific populations of synapses
546 in intact brain circuits. Combining circuit and super-resolution approaches through CLEM will
547 be critical to refine large-scale circuit models (Markram et al., 2015; Sarid et al., 2015; Bhatia
548 et al., 2019; but see Almog and Korngreen, 2016) and bridge the gap between molecular,
549 system and computational neurosciences.
550
551 **MATERIALS AND METHODS**

552 **Animals and *in utero* cortical electroporation**
553 All animals were handled according to French and EU regulations (APAFIS#1530-
554 2015082611508691v3). *In utero* cortical electroporation was performed as described
555 previously (Fossati et al., 2019). Briefly, pregnant Swiss female mice at E15.5 (Janvier Labs,
556 France) were anesthetized with isoflurane (3.5% for induction, 2% during the surgery) and
557 subcutaneously injected with 0.1 mg/kg of buprenorphine for analgesia. The uterine horns
558 were exposed after laparotomy. Electroporation was performed using a square wave
559 electroporator (ECM 830, BTX) and tweezer-type platinum disc electrodes (5mm-diameter,
560 Sonidel). The electroporation settings were: 4 pulses of 40 V for 50 ms with 500 ms interval.
561 Endotoxin-free DNA was injected using a glass pipette into one ventricle of the mouse
562 embryos at the following concentrations: pH1SCV2 TdTomato: 0.5 µg/µL and pCAG EGFP-
563 GPHN: 0.3 µg/µL. All constructs have been described before (Fossati et al., 2016).
564
565 **Cortical slice preparation**

566 Electroporated animals aged between postnatal day P84 and P129 were anesthetized with
567 ketamin 100 mg/kg and xylazin 10 mg/kg, and intracardiacally perfused with first 0.1 mL of
568 heparin (5000 U.I/mL, SANOFI), then an aqueous solution of 4% w/v paraformaldehyde (PFA)
569 (Clinisciences) and 0.5% glutaraldehyde (GA) (Clinisciences) in 0.1 M phosphate-buffered
570 saline (PBS). The fixative solution was made extemporaneously, and kept at ice-cold
571 temperature throughout the perfusion. The perfusion was gravity-driven at a flow rate of about
572 0.2 ml/s, and the total perfused volume was about 100 ml per animal. Brains were collected
573 and post-fixed overnight at 4°C in a 4% PFA solution. 30 µm-thick coronal brain sections were
574 obtained using a vibrating microtome (Leica VT1200S).
575
576 **Fluorescence microscopy of fixed tissue**
577 Slices containing electroporated neurons were trimmed to small (5-10 mm^2) pieces centered
578 on a relatively isolated fluorescent neuron, then mounted in a custom-made chamber on #1.5
579 glass coverslips. The mounting procedure consisted in enclosing the slices between the glass
580 coverslip and the bottom of a cell culture insert (Falcon, ref. 353095) adapted to the flat
581 surface with a silicon O-ring gasket (Leica) and fixed with fast-curing silicon glue
582 (Supplementary figure 1A). Volumes of GFP and tdTomato signals were acquired in 12 bits
583 mode (1024x1024 pixels) with z-steps of 400 nm using an inverted Leica TCS SP8 confocal
584 laser scanning microscope equipped with a tunable white laser and hybrid detectors and
585 controlled by the LAF AS software. The objective lenses were a 10X PlanApo, NA 0.45 lens
586 for identifying electroporated neurons and a 100X HC-PL APO, NA 1.44 CORR CS lens
587 (Leica) for higher magnification images. GFP-GPHN puncta with a peak signal intensity at
588 least four times above shot noise background levels were considered for CLEM.
589
590 **Placement of DAB fiducial landmarks**
591 Following confocal imaging, slices were immersed in a solution of 1 mg/mL 3,3'-
592 diaminobenzidine tetrahydrochloride (DAB, Sigma Aldrich) in Tris buffer (0.05 M, pH 7.4). The
593 plugin “LAS X FRAP” (Leica) was used to focus the pulsed laser in the tissue in custom
594 patterns of 10-to-20 points using 100% power in 4 wavelengths (470 to 494nm) for 30s-60s
595 per point at 3 different depths: the top of the slice, the depth of the targeted soma, then the
596 bottom of the slice (surface closest to the objective). DAB precipitates were imaged in
597 transmitted light mode. Slices were subsequently rinsed twice in Tris buffer and prepared for
598 electron microscopy.
599
600 **Tissue preparation for serial block-face scanning electron microscopy (SBEM)**
601 Using a scalpel blade under a M165FC stereomicroscope (Leica), imaged tissue slices were
602 cut to ~1mm^2 asymmetrical pieces of tissue centered on the ROI, and then kept in plastic

603 baskets (Leica) through the osmification and dehydration steps. Samples were treated using
604 an osmium bridging technique adapted from the NCMIR protocol (OTO) (Deerinck et al.,
605 2010). The samples were washed 3 times in ddH_2O and immersed for 1 hour in a reduced
606 osmium solution containing 2% osmium tetroxide and 1.5% potassium ferrocyanide in ddH_2O.
607 Samples were then immersed for 20 minutes in a 1% thiocarbohydrazide (TCH) solution
608 (Electron Microscopy Science) prepared in ddH_2O at room temperature. The samples were
609 then post-fixed with 2% OsO_4 in ddH_2O for 30 minutes at room temperature and colored *en*
610 *bloc* with 1% aqueous uranyl acetate at 4 °C during 12 hours. Post-fixed samples were
611 subjected to Walton's *en bloc* lead aspartate staining at 60 °C for 30 minutes (Walton, 1979).
612 After dehydration in graded concentrations of ice-cold ethanol solutions (20%, 50%, 70%,
613 90% and twice 100%, 5 minutes per step) the samples were rinsed twice for 10 minutes in
614 ice-cold anhydrous acetone. Samples were then infiltrated at room temperature with graded
615 concentrations of Durcupan (EMS) prepared without plastifier (components A, B, C only). In
616 detail, blocks were infiltrated with 25% Durcupan for 30 minutes, 50% Durcupan for 30
617 minutes, 75% Durcupan for 2 hours, 100% Durcupan overnight, and 100% fresh Durcupan
618 for 2 hours before being polymerized in a minimal amount of resin in a flat orientation in a
619 sandwich of ACLAR® 33C Films (EMS) at 60 °C for 48 hours. Samples were mounted on
620 aluminum pins using conductive colloidal silver glue (EMS). Before curing, tissue blocks were
621 pressed parallel to the pin surface using a modified glass knife with 0° clearance angle on an
622 ultramicrotome (Ultracut UC7, Leica), in order to minimize the angular mismatch between LM
623 and SEM imaging planes. Pins then cured overnight at 60°C. Samples were then trimmed
624 around the ROI with the help of fluorescent overviews of the ROI within their asymmetrical
625 shape. Minimal surfacing ensured that superficial DAB landmarks were detected at the SBEM
626 before block-facing.
627
628 **SBEM acquisition**
629 SBEM imaging was performed with a Teneo VS microscope (FEI) on the ImagoSeine imaging
630 platform at Institut Jacques Monod, Paris. The software MAPS (Leica) was used to acquire
631 SEM images of targeted volumes at various magnifications. Acquisition parameters were:
632 1,7830 kV, 500 ns/px, 100 pA, 40 nm-thick sectioning and 8200x8200 pixels resolution with
633 either 2.5 nm or 25 nm pixel size for high- and low-magnification images, respectively. Placing
634 an electromagnetic trap above the diamond knife to catch discarded tissue sections during
635 days-long imaging sessions was instrumental to achieve continuous 3DEM acquisitions.
636
637 **Image segmentation**
638 Dendrites were segmented from SBEM stacks using the software Microscopy Image Browser
639 (MIB) (Belevich et al., 2016). 3D reconstruction was performed with the software IMOD

640 (Kremer et al., 1996; http://bio3d.colorado.edu/imod/). 3D spine models were imported in the
641 software Blender (www.blender.org) for subsampling and the quantification of spine section
642 areas along their main axis was done with in-house python scripts. Other measurements were
643 performed using IMOD and in-house python scripts.
644
645 **Tissue preparation for tissue shrinkage estimation**
646 Two female mice (21 days postnatal) were used for the analysis of tissue shrinkage induced
647 by chemical fixation. Mice were decapitated and their brains were rapidly removed. The brains
648 were transferred to an ice-cold dissection medium, containing (in mM): KCl, 2.5; $NaHCO_3$, 25;
649 NaH_2PO_4, 1; $MgSO_4$, 8; glucose, 10, at pH 7.4. A mix of 95% O_2 and 5% CO_2 was bubbled
650 through the medium for 30 min before use. 300-µm-thick coronal brain sections were obtained
651 using a vibrating microtome (Leica VT1200S). Small fragments of the SSC were cut from
652 those slices and fixed either by immersion in an ice-cold PBS solution containing 4% PFA and
653 0.5% GA, or in frozen with liquid nitrogen under a pressure of 2100 bars using a high pressure
654 freezing system (HPM100, Leica). For HPF-frozen samples, the interval between removal of
655 the brain and vitrification was about 7 min. Cryo-substitution and tissue embedding were
656 performed in a Reichert AFS apparatus (Leica). Cryo-substitution was performed in acetone
657 containing 0.1% tannic acid at -90°C for 4 days with one change of solution, then in acetone
658 containing 2% osmium during the last 7h at -90°C. Samples were thawed slowly (5°C/h) to -
659 20°C and maintained at -20°C for 16 additional hours, then thawed to 4°C (10°C/h). At 4°C
660 the slices were immediately washed in pure acetone. Samples were rinsed several times in
661 acetone, then warmed to room temperature and incubated in 50% acetone-50% araldite
662 epoxy resin for 1h, followed by 10% acetone-90% araldite for 2h. Samples were then
663 incubated twice in araldite for 2h before hardening at 60°C for 48h. As for chemically fixed
664 sections, they were post-fixed for 30 min in ice-cold 2% osmium solution, rinsed in PBS buffer,
665 dehydrated in graded ice-cold ethanol solutions and rinsed twice in ice-cold acetone, before
666 undergoing the same resin infiltration and embedding steps as HPF-frozen samples. After
667 embedding, ultrathin sections were cut in L2/3 of the SSC, orthogonally to the apical dendrites
668 of pyramidal neurons, 200-300 µm from the pial surface using an ultramicrotome (Ultracut
669 UC7, Leica). Ultra-thin (pale yellow) sections were collected on formwar-coated nickel slot
670 grids, then counterstained with 5% uranyl acetate in 70% methanol for 10 min, washed in
671 distilled water and air dried before observation on a Philips TECNAI 12 electron microscope
672 (Thermo Fisher Scientific).
673
674 **Measurement of shrinkage correction factors**
675 Ultra-thin sections of both HPF-frozen tissues and chemically-fixed tissues were observed
676 using a Philips TECNAI 12 electron microscope (TFS). Cellular compartments contacted by a

pre-synaptic bouton containing synaptic vesicles and exhibiting a visible electron-dense PSD at the contact site, but no mitochondrion within their cytosol were identified as dendritic spine heads. Cross-section areas of random spine heads and the curvilinear lengths of their PSD were quantified in both conditions using the softwares MIB and IMOD. N = 277 spine head sections were segmented in HPF-frozen cortical slices from two female mice, and N = 371 spine head sections were segmented in chemically fixed cortical slices originating from the same two mice. Chi-square minimization was used between spine head cross-section area distributions in HPF or OTO conditions to compute average volume shrinkage and correction factors. PSD areas were not corrected as they exhibited no shrinkage.

Computation of the diffusional neck resistance

The diffusional resistance of spine necks W_{neck} was measured as follows. Using IMOD, we first modeled in 3D the principal axis of each spine neck as an open contour of total length L_{axis} connecting the base of the neck to the base of the spine head. Using Blender, we interpolated each spine neck path linearly with 100 points. We named P(l) the plane that bisected the spine neck model orthogonally to the path at the abscissa l, and A(l) the spine neck cross-section within P(l). In spines containing a spine apparatus (SA), we corrected A(l) by a scaling factor ß(l) = $1-(D_{SA}/D_{spine})^2(l)$, where $D_{SA}/D_{spine}(l)$ is the local ratio of SA and neck diameter. We measured D_{SA}/D_{spine} orthogonally to the neck path in 10 SA+ spines and in three different locations per spine on SBEM images: at the spine stem (l/L_{axis} = 0.1), at the center of the spine neck (l/L_{axis} = 0.5), and at the stem of the head (l/L_{axis} = 0.9). D_{SA}/D_{spine} was 44% ± 11%, 31% ± 8% and 37% ± 8% respectively, and fluctuations were not statistically significant. We then divided each SA+ spine neck in thirds and scaled their neck cross-section areas along neck axis $A_{SA+}(l)$ = ß(l)A(l) before computing $W_{neck} = \int dl/A(l)$ for all spines, using Simpson's integration rule.

Multi-compartment electrical model

All simulations were implemented in Python using NEURON libraries (Hines and Carnevale, 2001) and in-house scripts. Ordinary differential equations were solved with NEURON-default backward Euler method, with Δt = 0.05 ms. Scripts and model definition files are available in a GitHub repository: https://github.com/pabloserna/SpineModel. Biophysical constants were taken from the literature as follows: membrane capacitance C_m = 1μF/cm^2 (Doron et al., 2017); cytosolic resistivity ρ= 300 Ω.cm (Miceli et al., 2017; Barbour, 2017); synaptic conductivities were modeled as bi-exponential functions $g(t) = Ag_{max}(e^{-t/t_2} - e^{-t/t_1})$ where A is a normalizing constant and t_1 and t_2 define the kinetics of the synapses: GABAergic conductance (t_1, t_2) = (0.5, 15) ms, AMPAR-dependent conductance (t_1, t_2) = (0.1, 1.8) ms,

713 NMDAR-dependent conductance (t_1, t_2) = (0.5, 17.0) ms (ModelDB:
714 https://senselab.med.yale.edu/ModelDB/). The magnesium block of NMDA receptors was
715 modeled by a voltage-dependent factor (Jahr and Stevens, 1990). Remaining free parameters
716 comprised: the leaking conductivity g_m (or, equivalently, the membrane time constant T_m); the
717 peak synaptic conductance per area: g_{AMPA}, g_{NMDA}, g_{GABA}; the total membrane area of the
718 modeled neuron. These parameters were adjusted so that signal distributions fitted published
719 electrophysiological recordings (Feldmeyer et al., 2006; Kobayashi et al., 2008; Hull et al.,
720 2009; Avermann et al., 2012; Scala et al., 2018). In more detail, we first set up one "ball-and-
721 stick" model per segmented spine (N=390). The dendrite hosting the modeled spine was
722 generated as a tube of diameter $d_{dendrite}$ = 0.87 µm, and length $L_{dendrite}$ = 140 µm. This dendrite
723 is split in three parts, the 2 µm-long middle one harboring the modeled spine. To account for
724 the passive electrical effects of neighboring spines, the membrane surfaces of both the
725 proximal and distal sections of the studied dendrite were scaled by a correction factor alpha =
726 $1 + \langle A_{spine}\rangle d_{spine}/\pi d_{dendrite} = 3.34$, with the density d_{spine} =1.63 spine.µm^{-1} and the average spine
727 membrane area $\langle A_{sp}\rangle$ = 3.89 µm^2 . We calibrated synaptic conductances type by type, by
728 fitting the signals generated in the whole distribution of 390 models to published
729 electrophysiological recordings. The AMPA conductances of all excitatory synapses were set
730 proportional to ePSD area and scaled by the free parameter g_A. In each model, we activated
731 the AMPAR component of excitatory synapses and monitored the amplitude of resulting
732 EPSCs in the soma. The average EPSC amplitude was adjusted to 58 pA (Feldmeyer et al.,
733 2006; Hull et al., 2009), yielding a scaling factor g_A = 3.15 nS/µm^2, which takes into account
734 the average number of excitatory contacts per axon per PN in L2/3 of mouse SSC: $N_{ePSD/axon}$=
735 2.8 (Feldmeyer et al., 2006). The average AMPA synaptic conductance was 0.42 nS. The
736 leakage resistance was fitted to 65 MΩ (Hoffmann et al., 2015), yielding a total membrane
737 surface of the modeled neurons: $A_{mb,\ total}$ = 18550 µm^2. The NMDA conductances of all
738 excitatory synapses were set proportional to ePSD area and scaled by the free parameter g_N.
739 In each model, we activated both NMDA and AMPA components of excitatory synapses and
740 fitted the amplitude ratio between the average AMPA+NMDA and AMPA-only responses to
741 1.05 (Hull et al., 2009), yielding g_N = 3.4 nS/µm^2. The GABA conductances of all inhibitory
742 synapses were set proportional to iPSD area and scaled by the free parameter g_G. In this
743 case, we set the neuron to a holding potential of 0 mV and the reversal potential of chloride
744 ions (E_{Cl^-}) to -80 mV. Then, we activated shaft inhibitory synapses and monitored the
745 amplitude of resulting IPSCs in the soma. The amplitude of the average GABAergic
746 conductance was set to 1 nS (Doron et al., 2017; Hoffmann et al., 2015; Xu et al., 2013),
747 yielding a scaling factor g_G = 5.9 nS/µm^2, which takes into account the average number of
748 inhibitory contacts per axon per PN in L2/3 of mouse SSC: $N_{iPSD/axon}$ = 6 (Hoffmann et al.,
749 2015). Considering inhibition, since E_{Cl^-} is regulated on timescales exceeding 100 ms (Boffi et

750 al., 2018) and we modeled signals in the 10 ms timescale, we could set E_{Cl^-} as a constant
751 parameter of our steady state model. Calcium influxes were modeled in spines as a result of
752 the opening of NMDARs and voltage-dependent calcium channels (VDCCs). Since we
753 simulated signals that remained below the threshold for eliciting dendritic spikes (Sarid et al.,
754 2015; Stuart and Spruston, 2015), we did not include VDCCs in dendrites, and monitored
755 calcium transients exclusively in spine heads. The dynamics of L-, N- and Q-type VDCCs were
756 obtained from ModelDB (accession n°: 151458), and their conductivities were scaled to the
757 head membrane area of each spine, A_{head}, excluding synaptic area(s). VDCC-type ratios and
758 calcium conductivities were adjusted by fitting the average amplitude of calcium concentration
759 transients to 20% of the NMDA conductance (Bloodgood et al., 2009). Calcium uptake from
760 cytosolic buffers was set to 95% to yield an average amplitude of Ca^{2+} concentration transients
761 of 0.7 µM (Sabatini et al, 2002).
762
763 **Bootstrapping**
764 To simulate a large number of spine-spine interactions with limited redundancy, our
765 distribution of spines was expanded using a "smooth" bootstrapping method (Efron and
766 Tibshirani, 1994). Specifically, the dataset (i.e. a matrix of dimensions N x N_f) was re-sampled
767 to generate a new matrix of dimension M x N_f, where N is the number of spines, N_f is the
768 number of selected features, and M is the final number of synthetic spines. M rows were
769 randomly selected in the original dataset and zero-centered, feature-dependent Gaussian
770 noise was added to each element of the matrix (excluding absolute quantities, e.g. number of
771 PSDs or presence of SA). To determine appropriate noise amplitude for each parameter, a
772 synthetic set of M=500 spines was generated from the original dataset, including Gaussian
773 noise with an arbitrary amplitude σ, on one selected parameter. This new feature distribution
774 was compared to the original distribution using a 2-sample Kolmogorov-Smirnov test (KS-
775 test), and this procedure was repeated 1000 times for each set value of σ. A conservative
776 noise level (σ = 10%) was sufficient to smear parameter distributions while the fraction of
777 synthetic sets that were statistically different from the original set ($p < 0.05$, KS-test) remained
778 0 over 1000 iterations. σ = 10% was valid for all relevant features, and we assumed that such
779 a small noise amplitude would minimally interfere with non-linear correlations in our dataset.
780 Synthetically generated spines were then used to simulate elementary synaptic signaling
781 using in-house python scripts. We also used bootstrapping to estimate standard deviations in
782 our simulations.
783
784 **Statistics**
785 No statistical methods were used to predetermine sample size. We used a one-way ANOVA
786 on our 4 datasets (Supplementary table 1) to test that inter-neuron and inter-mice variability

were small enough to pool all datasets together (Supplementary table 2). We used Kolmogorov-Smirnov test to determine that all measured morphological parameters followed a log-normal distribution (Supplementary table 2). We used Mann–Whitney U test for statistical analyses of morphological parameters, except when comparing the probability for SiSs and DiSs to harbor SA, for which we used Pearson's χ^2 test. All results in the text are mean ± SD. In figures 6, 7 and 9, we plot medians as solid lines, as they better describe where log-normal distributions peak. Shaded areas represent 68% confidence intervals, which span approximately one standard deviation on each side of the mean.

ACKNOWLEDGEMENTS

We thank members of the Triller and Charrier laboratories (IBENS, Paris, France), Vincent Hakim and Boris Barbour for insightful discussions. This work was supported by INSERM, the Agence Nationale de la Recherche (ANR-13-PDOC-0003 and ANR-17-ERC3-0009 to C.C.), the European Research Council (ERC starting grant 803704 to C.C.), the Labex Memolife (901/IBENS/LD09 to O.G.), the company NIKON France via the CIFRE program (convention n° 2015/1049 to O.G.) and the European Union's Horizon 2020 Framework Programme for Research and Innovation under the Specific Grant Agreement No. 785907 (Human Brain Project SGA2 to P.S.). We acknowledge the ImagoSeine imaging facility (Jean-Marc Verbavatz and Rémi Leborgne, Jacques Monod Institute, Paris, France) for SBEM availability, service and support. We thank Liesbeth Hekkings (ThermoFisher Scientific) for technical support. We are grateful to the IBENS Imaging Facility (France BioImaging, supported by ANR-10-INBS-04, ANR-10-LABX-54 MEMO LIFE, and ANR-11-IDEX-000-02 PSL* Research University, ''Investments for the future''; NERF 2011-45; FRM DGE 20111123023; and FRC Rotary International France).

AUTHOR CONTRIBUTIONS

O.G. developed the 3D-CLEM workflow, performed the experiments, segmented images and analyzed data. P.S. coded the model and analyzed data. N.A. and M.F. carried out the *in utero* electroporations. P.R. trained O.G. in EM and carried out part of the TEM imaging. O.G., P.R., A.T. and C.C. designed the study. O.G., P.S. and C.C. interpreted the results, prepared the figures, and wrote the manuscript. A.T. and C.C. provided funding.

COMPETING INTERESTS

The authors declare that no competing interests exist.

REFERENCES

Acker, C. D., Hoyos, E., & Loew, L. M. (2016). EPSPs Measured in Proximal Dendritic Spines of Cortical Pyramidal Neurons. ENeuro, 3(2), 1–13. https://doi.org/10.1523/eneuro.0050-15.2016

Adrian, M., Kusters, R., Storm, C., Hoogenraad, C. C., & Kapitein, L. C. (2017). Probing the Interplay between Dendritic Spine Morphology and Membrane-Bound Diffusion. Biophysical Journal, 113(10), 2261–2270. https://doi.org/10.1016/j.bpj.2017.06.048

Almog, M., & Korngreen, A. (2014). A quantitative description of dendritic conductances and its application to dendritic excitation in layer 5 pyramidal neurons. Journal of Neuroscience, 34(1), 182–196. https://doi.org/10.1523/JNEUROSCI.2896-13.2014

Almog, M., & Korngreen, A. (2016). Is realistic neuronal modeling realistic? Journal of Neurophysiology, 116(5), 2180–2209. https://doi.org/10.1152/jn.00360.2016

Alvarez, V. A., & Sabatini, B. L. (2007). Anatomical and Physiological Plasticity of Dendritic Spines. Annual Review of Neuroscience, 30(1), 79–97. https://doi.org/10.1146/annurev.neuro.30.051606.094222

Araya, R., Vogels, T. P., & Yuste, R. (2014). Activity-dependent dendritic spine neck changes are correlated with synaptic strength. Proceedings of the National Academy of Sciences of the United States of America, 111(28). https://doi.org/10.1073/pnas.1321869111

Arellano, J. I. (2007). Ultrastructure of dendritic spines: correlation between synaptic and spine morphologies. Frontiers in Neuroscience, 1(1), 131–143. https://doi.org/10.3389/neuro.01.1.1.010.2007

Avermann, M., Tomm, C., Mateo, C., Gerstner, W., & Petersen, C. C. H. (2012). Microcircuits of excitatory and inhibitory neurons in layer 2/3 of mouse barrel cortex. Journal of Neurophysiology, 107(11), 3116–3134. https://doi.org/10.1152/jn.00917.2011

Bailey, C. H., Kandel, E. R., & Harris, K. M. (2015). Structural components of synaptic plasticity and memory consolidation. Cold Spring Harbor Perspectives in Biology, 7(7), 1–29. https://doi.org/10.1101/cshperspect.a021758

Ballesteros-Yáñez, I., Benavides-Piccione, R., Elston, G. N., Yuste, R., & DeFelipe, J. (2006). Density and morphology of 1 the Brain Extracellular Impedance Is High and Non-resistive. Biophysical Journal, 113(7), 1636–1638. https://doi.org/10.1016/j.bpj.2017.05.054

Barnes, S. A., Wijetunge, L. S., Jackson, A. D., Katsanevaki, D., Osterweil, E. K., Komiyama, N. H., … Wyllie, D. J. A. (2015). Convergence of hippocampal pathophysiology in syngap +/- and fmr 1-/y mice. Journal of Neuroscience, 35(45), 15073–15081. https://doi.org/10.1523/JNEUROSCI.1087-15.2015

Beaulieu, C., & Colonnier, M. (1985). A Laminar Analysis of the Number of Round-Asymmetrical and Flat- Symmetrical Synapses on Spines , Dendritic Trunks , and Cell Bodies in Area 17 of the Cat. Journal of Comparative Neurology, 189, 180–189.

Begemann, I., & Galic, M. (2016). Correlative light electron microscopy: Connecting synaptic structure and function. Frontiers in Synaptic Neuroscience, 8(AUG), 1–12. https://doi.org/10.3389/fnsyn.2016.00028

Belevich, I., Joensuu, M., Kumar, D., Vihinen, H., & Jokitalo, E. (2016). Microscopy Image Browser: A Platform for Segmentation and Analysis of Multidimensional Datasets. PLoS Biology, 14(1), 1–13. https://doi.org/10.1371/journal.pbio.1002340

Bell, M., Bartol, T., Sejnowski, T., & Rangamani, P. (2019). Dendritic spine geometry and spine apparatus organization govern the spatiotemporal dynamics of calcium. The Journal

of General Physiology, 151(9), 2221–2222. https://doi.org/10.1085/jgp.20181226107312019a

Berglund, K., Schleich, W., Wang, H., Feng, G., Hall, W. C., Kuner, T., & Augustine, G. J. (2008). Imaging synaptic inhibition throughout the brain via genetically targeted Clomeleon. Brain Cell Biology, 36(1–4), 101–118. https://doi.org/10.1007/s11068-008-9031-x

Bhatia, A., Moza, S., & Bhalla, U. S. (2019). Precise excitation-inhibition balance controls gain and timing in the hippocampus. ELife, 8, 1–29. https://doi.org/10.7554/eLife.43415

Bian, W. J., Miao, W. Y., He, S. J., Qiu, Z., & Yu, X. (2015). Coordinated Spine Pruning and Maturation Mediated by Inter-Spine Competition for Cadherin/Catenin Complexes. Cell, 162(4), 808–822. https://doi.org/10.1016/j.cell.2015.07.018

Bishop, D., Nikić, I., Brinkoetter, M., Knecht, S., Potz, S., Kerschensteiner, M., & Misgeld, T. (2011). Near-infrared branding efficiently correlates light and electron microscopy. Nature Methods, 8(7), 568–572. https://doi.org/10.1038/nmeth.1622

Blazquez-Llorca, L., Hummel, E., Zimmerman, H., Zou, C., Burgold, S., Rietdorf, J., & Herms, J. (2015). Correlation of two-photon in vivo imaging and FIB/SEM microscopy. Journal of Microscopy, 259(2), 129–136. https://doi.org/10.1007/978-3-319-95849-1_8

Bloodgood, B.L., Giessel, A.J. and Sabatini, B.L., 2009. Biphasic synaptic Ca influx arising from compartmentalized electrical signals in dendritic spines. PLoS biology, 7(9). https://doi.org/10.1371/journal.pbio.1000190

Boffi, J. C., Knabbe, J., Kaiser, M., & Kuner, T. (2018). KCC2-dependent steady-state intracellular chloride concentration and ph in cortical layer 2/3 neurons of anesthetized and awake mice. Frontiers in Cellular Neuroscience, 12(January), 1–14. https://doi.org/10.3389/fncel.2018.00007

Boivin, J. R., & Nedivi, E. (2018). Functional implications of inhibitory synapse placement on signal processing in pyramidal neuron dendrites. Current Opinion in Neurobiology, 51, 16–22. https://doi.org/10.1016/j.conb.2018.01.013

Bono, J., Wilmes, K. A., & Clopath, C. (2017). Modelling plasticity in dendrites: from single cells to networks. Current Opinion in Neurobiology, 46, 136–141. https://doi.org/10.1016/j.conb.2017.08.013

Bosch, C., Martínez, A., Masachs, N., Teixeira, C. M., Fernaud, I., Ulloa, F., … Soriano, E. (2015). FIB/SEM technology and high-throughput 3D reconstruction of dendritic spines and synapses in GFP-labeled adult-generated neurons. Frontiers in Neuroanatomy, 9. https://doi.org/10.3389/fnana.2016.00100

Bourne, J. N., & Harris, K. M. (2008). Balancing Structure and Function at Hippocampal Dendritic Spines. Annual Review of Neuroscience, 31(1), 47–67. https://doi.org/10.1146/annurev.neuro.31.060407.125646

Bourne, J. N., & Harris, K. M. (2011). Coordination of size and number of excitatory and inhibitory synapses results in a balanced. Hippocampus, 21(4), 354–373. https://doi.org/10.1002/hipo.20768.COORDINATION

Briggman, K. L., & Denk, W. (2006). Towards neural circuit reconstruction with volume electron microscopy techniques. Current Opinion in Neurobiology, 16(5), 562–570. https://doi.org/10.1016/j.conb.2006.08.010

Cane, M., Maco, B., Knott, G., & Holtmaat, A. (2014). The relationship between PSD-95 clustering and spine stability In Vivo. Journal of Neuroscience, 34(6), 2075–2086. https://doi.org/10.1523/JNEUROSCI.3353-13.2014

Chen, J. L., Villa, K. L., Cha, J. W., So, P. T. C., Kubota, Y., & Nedivi, E. (2012). Clustered Dynamics of Inhibitory Synapses and Dendritic Spines in the Adult Neocortex. Neuron, 74(2), 361–373. https://doi.org/10.1016/j.neuron.2012.02.030

Chirillo, M. A., Waters, M. S., Lindsey, L. F., Bourne, J. N., & Harris, K. M. (2019). Local resources of polyribosomes and SER promote synapse enlargement and spine clustering after long-term potentiation in adult rat hippocampus. Scientific Reports, 9(1), 1–14. https://doi.org/10.1038/s41598-019-40520-x

Chiu, C. Q., Barberis, A., & Higley, M. J. (2019). Preserving the balance: diverse forms of long-term GABAergic synaptic plasticity. Nature Reviews Neuroscience, 20(5), 272–281. https://doi.org/10.1038/s41583-019-0141-5

Chiu, C. Q., Lur, G., Morse, T. M., Carnevale, N. T., Ellis-Davies, G. C. R., & Higley, M. J. (2013). Compartmentalization of GABAergic inhibition by dendritic spines. Science, 340(6133), 759–762. https://doi.org/10.1126/science.1234274

Collman, F., Buchanan, J., Phend, K. D., Micheva, K. D., Weinberg, R. J., & Smith, S. J. (2015). Mapping Synapses by Conjugate Light-Electron Array Tomography. Journal of Neuroscience, 35(14), 5792–5807. https://doi.org/10.1523/JNEUROSCI.4274-14.2015

Dayan, P., & Abbott, L. F. (2001). Theoretical Neuroscience : Computational and Mathematical Modeling ofNeural Systems. In MIT Press.

De Boer, P., Hoogenboom, J. P., & Giepmans, B. N. G. (2015). Correlated light and electron microscopy: Ultrastructure lights up! Nature Methods, 12(6), 503–513. https://doi.org/10.1038/nmeth.3400

Deerinck, T. J., Bushong, E. A., Thor, A., & Ellisman, M. H. (2010). NCMIR Methods for 3D EM: A new protocol for preparation of biological specimens for serial block face scanning electron microscopy. Nat. Center Microsc. Imag. Res., 6.

Dehay, C., Douglas, R. J., Martin, K. A. C., & Nelson, C. (1991). Excitation by geniculocortical synapses is not “vetoed” at the level of dendritic spines in cat visual cortex. Journal of Physiology, 440, 723–734.

Doron, M., Chindemi, G., Muller, E., Markram, H., & Segev, I. (2017). Timed Synaptic Inhibition Shapes NMDA Spikes, Influencing Local Dendritic Processing and Global I/O Properties of Cortical Neurons. Cell Reports, 21(6), 1550–1561. https://doi.org/10.1016/j.celrep.2017.10.035

Doyon, N., Vinay, L., Prescott, S. A., & De Koninck, Y. (2016). Chloride Regulation: A Dynamic Equilibrium Crucial for Synaptic Inhibition. Neuron, 89(6), 1157–1172. https://doi.org/10.1016/j.neuron.2016.02.030

Efron, B., & Tibshirani, R. J. (1994). An Introduction to the Bootstrap. In CRC Press.

Elbohouty, M., Wilson, M. T., Voss, L. J., Steyn-Ross, D. A., & Hunt, L. A. (2013). In vitro electrical conductivity of seizing and non-seizing mouse brain slices at 10 kHz. Physics in Medicine & Biology, 58(11).

Feldmeyer, D., Lübke, J., & Sakmann, B. (2006). Efficacy and connectivity of intracolumnar pairs of layer 2/3 pyramidal cells in the barrel cortex of juvenile rats. Journal of Physiology, 575(2), 583–602. https://doi.org/10.1113/jphysiol.2006.105106

Feldmeyer, D. (2012). Excitatory neuronal connectivity in the barrel cortex. Frontiers in Neuroanatomy, 6(July), 1–22. https://doi.org/10.3389/fnana.2012.00024

Fifková, E., & Anderson, C. L. (1981). Stimulation-induced changes in dimensions of stalks of dendritic spines in the dentate molecular layer. Experimental Neurology, 74(2), 621–627. https://doi.org/10.1016/0014-4886(81)90197-7

Fifková, E., Eason, H., & Schaner, P. (1992). Inhibitory contacts on dendritic spines of the dentate fascia. Brain Research, 577(2), 331–336. https://doi.org/10.1016/0006-8993(92)90293-I

Forrest, M. P., Parnell, E., & Penzes, P. (2018). Dendritic structural plasticity and neuropsychiatric disease. Nature Reviews Neuroscience, 19(4), 215–234. https://doi.org/10.1038/nrn.2018.16

Fossati, M., Assendorp, N., Gemin, O., Colasse, S., Dingli, F., Arras, G., … Charrier, C. (2019). Trans-Synaptic Signaling through the Glutamate Receptor Delta-1 Mediates Inhibitory Synapse Formation in Cortical Pyramidal Neurons. Neuron, 104(6). https://doi.org/10.1016/j.neuron.2019.09.027

Fossati, M., Pizzarelli, R., Schmidt, E. R., Kupferman, J. V., Stroebel, D., Polleux, F., & Charrier, C. (2016). SRGAP2 and Its Human-Specific Paralog Co-Regulate the Development of Excitatory and Inhibitory Synapses. Neuron, 91(2), 356–369. https://doi.org/10.1016/j.neuron.2016.06.013

Frenkel, M. Y., Sawtell, N. B., Diogo, A. C. M., Yoon, B., Neve, R. L., & Bear, M. F. (2006). Instructive Effect of Visual Experience in Mouse Visual Cortex. Neuron, 51(3), 339–349. https://doi.org/10.1016/j.neuron.2006.06.026

Gabernet, L., Jadhav, S. P., Feldman, D. E., Carandini, M., & Scanziani, M. (2005). Somatosensory integration controlled by dynamic thalamocortical feed-forward inhibition. Neuron, 48(2), 315–327. https://doi.org/10.1016/j.neuron.2005.09.022

Gidon, A., & Segev, I. (2012). Principles Governing the Operation of Synaptic Inhibition in Dendrites. Neuron, 75(2), 330–341. https://doi.org/10.1016/j.neuron.2012.05.015

Globus, A., Rosenzweig, M., Bennett, E., & Diamond, M. (1973). Effects of differential experience on dendritic spine counts in rat cerebral cortex. Comp Physiol Psychol., 82(Feb), 175–181.

Gulledge, A. T., Carnevale, N. T., & Stuart, G. J. (2012). Electrical advantages of dendritic spines. PLoS ONE, 7(4). https://doi.org/10.1371/journal.pone.0036007

Hao, J., Wang, X. D., Dan, Y., Poo, M. M., & Zhang, X. H. (2009). An arithmetic rule for spatial summation of excitatory and inhibitory inputs in pyramidal neurons. Proceedings of the National Academy of Sciences of the United States of America, 106(51), 21906–21911. https://doi.org/10.1073/pnas.0912022106

Harnett, M. T., Makara, J. K., Spruston, N., Kath, W. L., & Magee, J. C. (2012). Synaptic amplification by dendritic spines enhances input cooperativity. Nature, 491(7425), 599–602. https://doi.org/10.1038/nature11554

Harris, K. M., Spacek, J., Bell, M. E., Parker, P. H., Lindsey, L. F., Baden, A. D., … Burns, R. (2015). A resource from 3D electron microscopy of hippocampal neuropil for user training and tool development. Scientific Data, 2, 1–19. https://doi.org/10.1038/sdata.2015.46

Harris, K. M., & Stevens, J. K. (1989). Dendritic spines of CA1 pyramidal cells in the rat hippocampus: Serial electron microscopy with reference to their biophysical characteristics. Journal of Neuroscience, 9(8), 2982–2997. https://doi.org/10.1523/jneurosci.09-08-02982.1989

Harris, K. M., & Weinberg, R. J. (2012). Ultrastructure of Synapses in the Mammalian Brain Ultrastructure of Synapses in the. Cold Spring Harb Perspect Biol. https://doi.org/10.1101/cshperspect.a005587

Hayama, T., Noguchi, J., Watanabe, S., Takahashi, N., Hayashi-Takagi, A., Ellis-Davies, G. C. R., … Kasai, H. (2013). GABA promotes the competitive selection of dendritic spines by controlling local Ca 2+ signaling. Nature Neuroscience, 16(10), 1409–1416. https://doi.org/10.1038/nn.3496

Hayashi-Takagi, A., Yagishita, S., Nakamura, M., Shirai, F., Wu, Y. I., Loshbaugh, A. L., … Kasai, H. (2015). Labelling and optical erasure of synaptic memory traces in the motor cortex. Nature, 525(7569), 333–338. https://doi.org/10.1038/nature15257

Helmstaedter, M. (2013). Cellular-resolution connectomics: Challenges of dense neural circuit reconstruction. Nature Methods, 10(6), 501–507. https://doi.org/10.1038/nmeth.2476

Herculano-Houzel, S., Watson, C., & Paxinos, G. (2013). Distribution of neurons in functional areas of the mouse cerebral cortex reveals quantitatively different cortical zones. Frontiers in Neuroanatomy, 7(OCT), 1–14. https://doi.org/10.3389/fnana.2013.00035

Hersch, S. M., & White, E. L. (1981). Quantification of synapses formed with apical dendrites of golgi-impregnated pyramidal cells: Variability in thalamocortical inputs, but consistency in the ratios of asymmetrical to symmetrical synapses. Neuroscience, 6(6). https://doi.org/10.1016/0306-4522(81)90069-5

Higley, M. J. (2014). Localized GABAergic inhibition of dendritic Ca2+ signalling. Nature Reviews Neuroscience, 15(9), 567–572. https://doi.org/10.1038/nrn3803

Hines, M. L., & Carnevale, N. T. (2001). NEURON: A tool for neuroscientists. Neuroscientist, 7(2), 123–135. https://doi.org/10.1177/107385840100700207

Hodgkin, A. L., & Huxley, A. F. (1952). A quantitative description of membrane current and its application to conduction and excitation in nerve. J. Physiol. (London), 117, 500–544. https://doi.org/10.1109/ICCCT2.2017.7972284

Hoffmann, J. H. O., Meyer, H. S., Schmitt, A. C., Straehle, J., Weitbrecht, T., Sakmann, B., & Helmstaedter, M. (2015). Synaptic conductance estimates of the connection between local inhibitor interneurons and pyramidal neurons in layer 2/3 of a cortical column. Cerebral Cortex, 25(11), 4415–4429. https://doi.org/10.1093/cercor/bhv039

Holderith, N., Lorincz, A., Katona, G., Rózsa, B., Kulik, A., Watanabe, M., & Nusser, Z. (2012). Release probability of hippocampal glutamatergic terminals scales with the size of the active zone. Nature Neuroscience, 15(7), 988–997. https://doi.org/10.1038/nn.3137

Honkura, N., Matsuzaki, M., Noguchi, J., Ellis-Davies, G. C. R., & Kasai, H. (2008). The Subspine Organization of Actin Fibers Regulates the Structure and Plasticity of Dendritic Spines. Neuron, 57(5), 719–729. https://doi.org/10.1016/j.neuron.2008.01.013

Hull, C., Isaacson, J. S., & Scanziani, M. (2009). Postsynaptic Mechanisms Govern the Differential Excitation of Cortical Neurons by Thalamic Inputs. Journal of Neuroscience, 29(28), 9127–9136. https://doi.org/10.1523/jneurosci.5971-08.2009

Iascone, D. M., Li, Y., Sümbül, U., Doron, M., Chen, H., Andreu, V., … Polleux, F. (2020). Whole-Neuron Synaptic Mapping Reveals Spatially Precise Excitatory/Inhibitory Balance Limiting Dendritic and Somatic Spiking. Neuron, 1–13. https://doi.org/10.1016/j.neuron.2020.02.015

Isaacson, J. S., & Scanziani, M. (2011). How inhibition shapes cortical activity. Neuron, 72(2), 231–243. https://doi.org/10.1016/j.neuron.2011.09.027

Jahr, C. E., & Stevens, C. F. (1990). A quantitative description of NMDA receptor-channel kinetic behavior. Journal of Neuroscience, 10(6), 1830–1837. https://doi.org/10.1523/jneurosci.10-06-01830.1990

Jayant, K., Hirtz, J. J., Plante, I. J. La, Tsai, D. M., De Boer, W. D. A. M., Semonche, A., … Yuste, R. (2017). Targeted intracellular voltage recordings from dendritic spines using quantum-dot-coated nanopipettes. Nature Nanotechnology, 12(4), 335–342. https://doi.org/10.1038/nnano.2016.268

Jones, E. G., & Powell, T. P. (1969). Morphological variations in the dendritic spines of the neocortex. Journal of Cell Science, 5(2), 509–529. Retrieved from http://www.ncbi.nlm.nih.gov/pubmed/5362339

Karreman, M. A., Hyenne, V., Schwab, Y., & Goetz, J. G. (2016). Intravital Correlative Microscopy: Imaging Life at the Nanoscale. Trends in Cell Biology, 26(11), 848–863. https://doi.org/10.1016/j.tcb.2016.07.003

1061 Kasthuri, N., Hayworth, K. J., Berger, D. R., Schalek, R. L., Conchello, J. A., Knowles-Barley,
1062 S., … Lichtman, J. W. (2015). Saturated Reconstruction of a Volume of Neocortex. Cell,
1063 162(3), 648–661. https://doi.org/10.1016/j.cell.2015.06.054
1064 Katz, Y., Menon, V., Nicholson, D. A., Geinisman, Y., Kath, W. L., & Spruston, N. (2009).
1065 Synapse Distribution Suggests a Two-Stage Model of Dendritic Integration in CA1 Pyramidal
1066 Neurons. Neuron, 63(2), 171–177. https://doi.org/10.1016/j.neuron.2009.06.023
1067 Kennedy, M. J., & Hanus, C. (2019). Architecture and Dynamics of the Neuronal Secretory
1068 Network. Annual Review of Cell and Developmental Biology, 35(1), 1–24.
1069 https://doi.org/10.1146/annurev-cellbio-100818-125418
1070 Knott, G. W., Holtmaat, A., Wilbrecht, L., Welker, E., & Svoboda, K. (2006). Spine growth
1071 precedes synapse formation in the adult neocortex in vivo. Nature Neuroscience, 9(9), 1117–
1072 1124. https://doi.org/10.1038/nn1747
1073 Knott, G. W., Quairiaux, C., Genoud, C., & Welker, E. (2002). Formation of Dendritic Spines
1074 with GABAergic Synapses Induced by Whisker Stimulation in Adult Mice. Neuron, 34, 265–
1075 273. https://doi.org/10.1016/S0896-6273(02)00663-3
1076 Kobayashi, M., Hamada, T., Kogo, M., Yanagawa, Y., Obata, K., & Kang, Y. (2008).
1077 Developmental profile of GABAA-mediated synaptic transmission in pyramidal cells of the
1078 somatosensory cortex. European Journal of Neuroscience, 28(5), 849–861.
1079 https://doi.org/10.1111/j.1460-9568.2008.06401.x
1080 Koch, C., Poggio, T., & Torre, V. (1983). Nonlinear interactions in a dendritic tree: localization,
1081 timing, and role in information processing. Proceedings of the National Academy of Sciences
1082 of the United States of America, 80(9), 2799–2802. https://doi.org/10.1073/pnas.80.9.2799
1083 Korkotian, E., Frotscher, M., & Segal, M. (2014). Synaptopodin regulates spine plasticity:
1084 Mediation by calcium stores. Journal of Neuroscience, 34(35), 11641–11651.
1085 https://doi.org/10.1523/JNEUROSCI.0381-14.2014
1086 Korogod, N., Petersen, C. C. H., & Knott, G. W. (2015). Ultrastructural analysis of adult mouse
1087 neocortex comparing aldehyde perfusion with cryo fixation. ELife, 4(AUGUST2015), 1–17.
1088 https://doi.org/10.7554/eLife.05793
1089 Kremer, J. R., Mastronarde, D. N., & McIntosh, J. R. (1996). Computer visualization of three-
1090 dimensional image data using IMOD. Journal of Structural Biology, 116(1), 71–76.
1091 https://doi.org/10.1006/jsbi.1996.0013
1092 Krueger-Burg, D., Papadopoulos, T., & Brose, N. (2017). Organizers of inhibitory synapses
1093 come of age. Current Opinion in Neurobiology, 45, 66–77.
1094 https://doi.org/10.1016/j.conb.2017.04.003
1095 Kubota, Y., Karube, F., Nomura, M., & Kawaguchi, Y. (2016). The Diversity of Cortical
1096 Inhibitory Synapses. Frontiers in Neural Circuits, 10(April), 1–15.
1097 https://doi.org/10.3389/fncir.2016.00027
1098 Kubota, Y., Kondo, S., Nomura, M., Hatada, S., Yamaguchi, N., Mohamed, A. A., …
1099 Kawaguchi, Y. (2015). Functional effects of distinct innervation styles of pyramidal cells by
1100 fast spiking cortical interneurons. ELife, 4(July 2015), 1–27.
1101 https://doi.org/10.7554/eLife.07919
1102 Kubota, Y., van Rijnsoever, C., Kondo, S., Karube, F., & Kawaguchi, Y. (2007). Neocortical
1103 Inhibitory Terminals Innervate Dendritic Spines Targeted by Thalamocortical Afferents.
1104 Journal of Neuroscience, 27(5), 1139–1150. https://doi.org/10.1523/JNEUROSCI.3846-
1105 06.2007
1106 Kuljis, D. A., Park, E., Telmer, C. A., Lee, J., Ackerman, D. S., Bruchez, M. P., & Barth, A. L.
1107 (2019). Fluorescence-based quantitative synapse analysis for cell-type specific
1108 connectomics. ENeuro. https://doi.org/10.1523/ENEURO.0193-19.2019

Lagache, T., Jayant, K., & Yuste, R. (2019). Electrodiffusion models of synaptic potentials in dendritic spines. Journal of Computational Neuroscience, 47(1), 77–89.

Larkum, M. E. (2009). Synaptic Integration in Tuft Dendrites. Science, 325(2009), 756–761. https://doi.org/10.1126/science.1171958

Lees, R. M., Peddie, C. J., Collinson, L. M., Ashby, M. C., & Verkade, P. (2017). Correlative two-photon and serial block face scanning electron microscopy in neuronal tissue using 3D near-infrared branding maps. In Methods in Cell Biology (Vol. 140). https://doi.org/10.1016/bs.mcb.2017.03.007

Lefort, S., Tomm, C., Floyd Sarria, J. C., & Petersen, C. C. H. (2009). The Excitatory Neuronal Network of the C2 Barrel Column in Mouse Primary Somatosensory Cortex. Neuron, 61(2), 301–316. https://doi.org/10.1016/j.neuron.2008.12.020

Lisman, J. (1989). A mechanism for the Hebb and the anti-Hebb processes underlying learning and memory. Proceedings of the National Academy of Sciences of the United States of America, 86(23), 9574–9578. https://doi.org/10.1073/pnas.86.23.9574

Losonczy, A., Makara, J. K., & Magee, J. C. (2008). Compartmentalized dendritic plasticity and input feature storage in neurons. Nature, 452(7186), 436–441. https://doi.org/10.1038/nature06725

Luckner, M., Burgold, S., Filser, S., Scheungrab, M., Niyaz, Y., Hummel, E., … Herms, J. (2018). Label-free 3D-CLEM Using Endogenous Tissue Landmarks. iScience, 6, 92–101. https://doi.org/10.1016/j.isci.2018.07.012

Maclachlan, C., Sahlender, D. A., Hayashi, S., Molnár, Z., & Knott, G. (2018). Block Face Scanning Electron Microscopy of Fluorescently Labeled Axons Without Using Near Infra-Red Branding. Frontiers in Neuroanatomy, 12(November), 1–8. https://doi.org/10.3389/fnana.2018.00088

Maco, B., Holtmaat, A., Cantoni, M., Kreshuk, A., Straehle, C. N., Hamprecht, F. A., & Knott, G. W. (2013). Correlative In Vivo 2 Photon and Focused Ion Beam Scanning Electron Microscopy of Cortical Neurons. PLoS ONE, 8(2), 1–7. https://doi.org/10.1371/journal.pone.0057405

Markram, H., Muller, E., Ramaswamy, S., Reimann, M. W., Abdellah, M., Sanchez, C. A., … Schürmann, F. (2015). Reconstruction and Simulation of Neocortical Microcircuitry. Cell, 163(2), 456–492. https://doi.org/10.1016/j.cell.2015.09.029

Matsuzaki, M., Honkura, N., Ellis-Davies, G. C. R., & Kasai, H. (2004). Structural basis of long-term potentiation in single dendritic spines. Nature, 429, 761–766. https://doi.org/10.1038/255243a0

Meißlitzer-Ruppitsch, C., Röhrl, C., Neumüller, J., Pavelka, M., & Ellinger, A. (2009). Photooxidation technology for correlated light and electron microscopy. Journal of Microscopy, 235(3), 322–335. https://doi.org/10.1111/j.1365-2818.2009.03220.x

Miceli, S., Ness, T. V., Einevoll, G. T., & Schubert, D. (2017). Impedance Spectrum in Cortical Tissue: Implications for Propagation of LFP Signals on the Microscopic Level. Eneuro, 4(1), ENEURO.0291-16.2016. https://doi.org/10.1523/eneuro.0291-16.2016

Micheva, K. D., & Beaulieu, C. (1995). Anatomical substrate for experience-dependent plasticity of the rat barrel field cortex. PNAS, 92(December), 11834–11838.

Motta, A., Berning, M., Boergens, K. M., Staffler, B., Beining, M., Loomba, S., … Helmstaedter, M. (2019). Dense connectomic reconstruction in layer 4 of the somatosensory cortex. Science, 366(6469). https://doi.org/10.1126/science.aay3134

Müller-Reichert, T., & Verkade, P. (2017). Correlative Light and Electron Microscopy III. In Methods in Cell Biology (Vol. 140).

Müllner, F. E., Wierenga, C. J., & Bonhoeffer, T. (2015). Precision of Inhibition: Dendritic Inhibition by Individual GABAergic Synapses on Hippocampal Pyramidal Cells Is Confined in Space and Time. Neuron, 87(3), 577–590. https://doi.org/10.1016/j.neuron.2015.07.003

Nabavi, S., Fox, R., Proulx, C. D., Lin, J. Y., Tsien, R. Y., & Malinow, R. (2014). Engineering a memory with LTD and LTP. Nature, 511(7509), 348–352. https://doi.org/10.1038/nature13294

Nakahata, Y., & Yasuda, R. (2018). Plasticity of spine structure: Local signaling, translation and cytoskeletal reorganization. Frontiers in Synaptic Neuroscience, 10(AUG), 1–13. https://doi.org/10.3389/fnsyn.2018.00029

Nevian, T., Larkum, M. E., Polsky, A., & Schiller, J. (2007). Properties of basal dendrites of layer 5 pyramidal neurons: A direct patch-clamp recording study. Nature Neuroscience, 10(2), 206–214. https://doi.org/10.1038/nn1826

Noguchi, J., Matsuzaki, M., Ellis-Davies, G. C. R., & Kasai, H. (2005). Spine-neck geometry determines NMDA receptor-dependent Ca2+ signaling in dendrites. Neuron, 46(4), 609–622. https://doi.org/10.1016/j.neuron.2005.03.015

Noguchi, J., Nagaoka, A., Watanabe, S., Ellis-Davies, G. C. R., Kitamura, K., Kano, M., … Kasai, H. (2011). In vivo two-photon uncaging of glutamate revealing the structure-function relationships of dendritic spines in the neocortex of adult mice. The Journal of Physiology, 589(10), 2447–2457. https://doi.org/10.1113/jphysiol.2011.207100

Nusser, Z., Cull-Candy, S., & Farrant, M. (1997). Differences in synaptic GABAA receptor number underlie variation in GABA mini amplitude. Neuron, 19, 697–709.

Nusser, Z., Hájos, N., Somogyi, P., & Mody, I. (1998). Increased number of synaptic GABAA receptors underlies potentiation at hippocampal inhibitory synapses. Nature, 395, 172–177.

Pedregosa, F., Varoquaux, G., Gramfort, A., Michel, V., Thirion, B., Grisel, O., … Duchesnay, É. (2011). Scikit-Learn: Machine Learning in Python. Journal of Machine Learning Research, 12(Oct), 2825–2830.

Poirazi, P., & Papoutsi, A. (2020). Illuminating dendritic function with computational models. Nature Reviews Neuroscience. https://doi.org/10.1038/s41583-020-0301-7

Popovic, M. A., Carnevale, N., Rozsa, B., & Zecevic, D. (2015). Electrical behaviour of dendritic spines as revealed by voltage imaging. Nature Communications. https://doi.org/10.1038/ncomms9436

Rajkovich, K. E., Loerwald, K. W., Hale, C. F., Hess, C. T., Gibson, J. R., & Huber, K. M. (2017). Experience-Dependent and Differential Regulation of Local and Long-Range Excitatory Neocortical Circuits by Postsynaptic Mef2c. Neuron, 93(1), 48–56. https://doi.org/10.1016/j.neuron.2016.11.022

Rall, W. (1964). Theoretical significance of dendritic trees for neuronal input-output relations. Neural Theory and Modeling, 73–97.

Rall, W. (1970). Cable properties of dendrites and effects of synaptic location. Excitatory Synaptic Mechanisms, 175–187.

Ramon y Cajal, S. (1899). Regias y consejos sobre investigacion biologica. Madrid Imprenta de Fontanet.

Rostaing, P., Real, E., Siksou, L., Lechaire, J. P., Boudier, T., Boeckers, T. M., … Marty, S. (2006). Analysis of synaptic ultrastructure without fixative using high-pressure freezing and tomography. European Journal of Neuroscience, 24(12), 3463–3474. https://doi.org/10.1111/j.1460-9568.2006.05234.x

Sabatini, B. L., Oertner, T. G., & Svoboda, K. (2002). The life cycle of Ca2+ ions in dendritic spines. Neuron, 33(3), 439-452. https://doi.org/10.1016/S0896-6273(02)00573-1

Sanes, J. R., & Zipursky, S. L. (2020). Synaptic Specificity, Recognition Molecules, and Assembly of Neural Circuits. Cell, 181(3), 536–556. https://doi.org/10.1016/j.cell.2020.04.008

Sarid, L., Bruno, R., Sakmann, B., Segev, I., & Feldmeyer, D. (2007). Modeling a layer 4-to-layer 2/3 module of a single column in rat neocortex: Interweaving in vitro and in vivo experimental observations. Proceedings of the National Academy of Sciences, 104(41), 16353–16358. https://doi.org/10.1073/pnas.0707853104

Sarid, L., Feldmeyer, D., Gidon, A., Sakmann, B., & Segev, I. (2015). Contribution of intracolumnar layer 2/3-to-Layer 2/3 excitatory connections in shaping the response to whisker deflection in rat barrel cortex. Cerebral Cortex, 25(4), 849–858. https://doi.org/10.1093/cercor/bht268

Scala, F., Kobak, D., Shan, S., Bernaerts, Y., Laturnus, S., Cadwell, C. R., … Tolias, A. S. (2018). Neocortical layer 4 in adult mouse differs in major cell types and circuit organization between primary sensory areas. BioRxiv. https://doi.org/http://dx.doi.org/10.1101/507293

Schüz, A., & Palm, G. (1989). Density of neurons and synapses in the cerebral cortex of the mouse. Journal of Comparative Neurology, 286(4), 442–455. https://doi.org/10.1002/cne.902860404

Segal, M. (2017). Dendritic spines: Morphological building blocks of memory. Neurobiology of Learning and Memory, 138, 3–9. https://doi.org/10.1016/j.nlm.2016.06.007

Segal, M., & Korkotian, E. (2014). Endoplasmic reticulum calcium stores in dendritic spines. Frontiers in Neuroanatomy, 8(JULY), 1–7. https://doi.org/10.3389/fnana.2014.00064

Segev, I., & Rall, W. (1988). Computational Study of an Excitable Dendritic Spine. In Journal of Neurophysiology (Vol. 60). Retrieved from http://jn.physiology.org/

Spacek, J., & Harris, K. M. (1997). Three-dimensional organization of smooth endoplasmic reticulum in hippocampal CA1 dendrites and dendritic spines of the immature and mature rat. Journal of Neuroscience, 17(1), 190–203. https://doi.org/10.1523/jneurosci.17-01-00190.1997

Stuart, G., & Spruston, N. (2015). Dendritic integration: 60 years of progress. Nature Neuroscience, 18(12), 1713–1721. https://doi.org/10.1038/nn.4157

Stuart, G., Spruston, N., & Häusser, M. (2016). Dendrites. In Oxford University Press.

Svoboda, K., Tank, D. W., & Denk, W. (1996). Direct measurement of coupling between dendritic spines and shafts. Science, 272(5262), 716–719. https://doi.org/10.1126/science.272.5262.716

Takasaki, K., & Sabatini, B. L. (2014). Super-resolution 2-photon microscopy reveals that the morphology of each dendritic spine correlates with diffusive but not synaptic properties. Frontiers in Neuroanatomy, 8(May), 1–7. https://doi.org/10.3389/fnana.2014.00029

Tønnesen, J., Katona, G., Rózsa, B., & Nägerl, U. V. (2014). Spine neck plasticity regulates compartmentalization of synapses. Nature Neuroscience, 17(5), 678–685. https://doi.org/10.1038/nn.3682

Tønnesen, J., & Nägerl, U. V. (2016). Dendritic spines as tunable regulators of synaptic signals. Frontiers in Psychiatry, 7(JUN). https://doi.org/10.3389/fpsyt.2016.00101

Tyagarajan, S. K., & Fritschy, J. M. (2014). Gephyrin: A master regulator of neuronal function? Nature Reviews Neuroscience, 15(3), 141–156. https://doi.org/10.1038/nrn3670

van Versendaal, D., Rajendran, R., Saiepour, H. M., Klooster, J., Smit-Rigter, L., Sommeijer, J. P., … Levelt, C. N. (2012). Elimination of Inhibitory Synapses Is a Major Component of Adult Ocular Dominance Plasticity. Neuron, 74(2), 374–383. https://doi.org/10.1016/j.neuron.2012.03.015

Villa, K. L., Berry, K. P., Subramanian, J., Cha, J. W., Oh, W. C., Kwon, H. B., … Nedivi, E. (2016). Inhibitory Synapses Are Repeatedly Assembled and Removed at Persistent Sites In Vivo. Neuron, 89(4), 756–769. https://doi.org/10.1016/j.neuron.2016.01.010

Walton, J. (1979). Lead an en Bloc Contrast Stain Particularly Ultrastructural Enzymology ' Useful for. Health (San Francisco).

Wehr, M., & Zador, A. M. (2003). Balanced inhibition underlies. Letters to Nature, 426(November), 860–863.

Williams, S. R., & Stuart, G. J. (2003). Role of dendritic synapse location in the control of action potential output. Trends in Neurosciences, 26(3), 147–154. https://doi.org/10.1016/S0166-2236(03)00035-3

Xu, H., Jeong, H. Y., Tremblay, R., & Rudy, B. (2013). Neocortical Somatostatin-Expressing GABAergic Interneurons Disinhibit the Thalamorecipient Layer 4. Neuron, 77(1), 155–167. https://doi.org/10.1016/j.neuron.2012.11.004

Yasuda, R. (2017). Biophysics of Biochemical Signaling in Dendritic Spines: Implications in Synaptic Plasticity. Biophysical Journal, 113(10), 2152–2159. https://doi.org/10.1016/j.bpj.2017.07.029

Yuste, R. (2013). Electrical Compartmentalization in Dendritic Spines. Annual Review of Neuroscience, 36(1), 429–449. https://doi.org/10.1146/annurev-neuro-062111-150455

Yuste, R., & Bonhoeffer, T. (2004). Genesis of dendritic spines: Insights from ultrastructural and imaging studies. Nature Reviews Neuroscience, 5(1), 24–34. https://doi.org/10.1038/nrn1300

Yuste, R., Majewska, A., & Holthoff, K. (2000). From form to function: Calcium compartmentalization in dendritic spines. Nature Neuroscience, 3(7), 653–659. https://doi.org/10.1038/76609

FIGURES AND LEGENDS

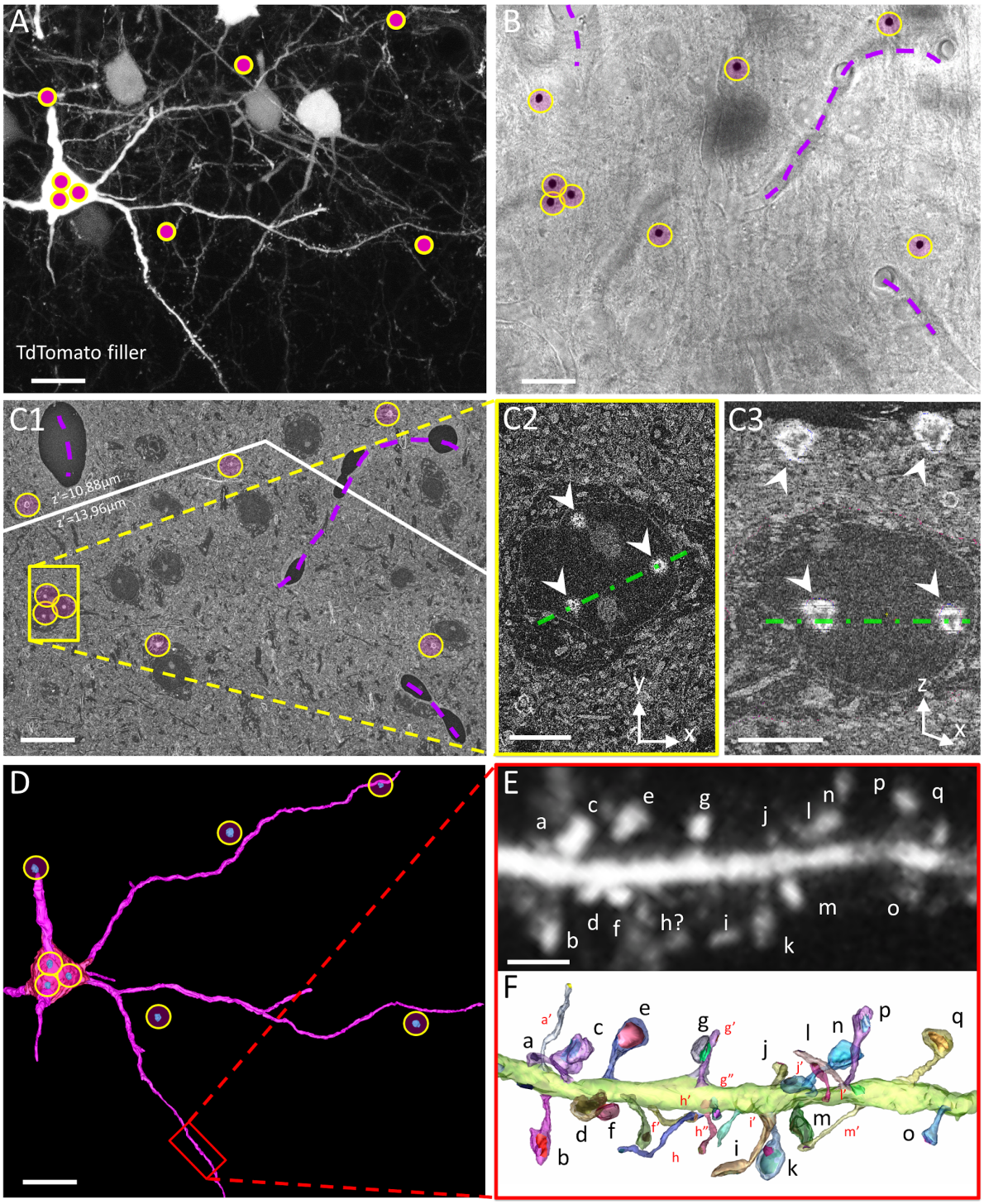

Figure 1. CLEM imaging of identified spines within intact cortical circuits.

(A) Visualization of basal dendrites of a pyramidal neuron expressing cytosolic TdTomato in layers 2/3 (L2/3) of adult mouse somatosensory cortex. Diaminobenzidine (DAB) was photo-precipitated using focused UV light to insert correlative landmarks (pink dots in yellow circles).

(B) Transmitted light image of the same field of view after DAB photo-precipitation. DAB precipitates are highlighted with yellow circles. Blood vessels are outlined with purple dashed lines.

(C) Composite scanning EM (SEM) image displaying DAB patterning at the depth of the neuron of interest (yellow circles). Slight mismatch between LM and SEM observation planes resulted in DAB landmarks appearing in different z-planes during block-facing; the white line represents stitching between z-shifted images. In C1, landmarks are arranged as in B. C2 is a close-up on the soma of the electroporated neuron, labelled with three DAB landmarks (arrowheads). C3 corresponds to an orthogonal (x,z) view of the SEM stack along the green dashed line in C2. The superficial DAB layer enabled ROI targeting, and the deeper layer enabled retrospective identification of the target neuron.

(D) 3D-reconstruction of dendrites of interest from the overview SEM stack. DAB landmarks are reconstructed in blue (in yellow circles). The red rectangle outlines the portion of dendrite represented in E and F.

(E) Z-projection of the confocal stack corresponding to the portion of dendrite reconstructed in D. Letters identify individual spines.

(F) 3D-EM reconstruction. Individual dendritic spines are manually segmented and randomly colored. Spines that were detected in EM but not in LM are labelled in red.

Scale bars: A, B, C1, D: 10 µm; C2, C3: 5 µm; E, F: 2 µm.

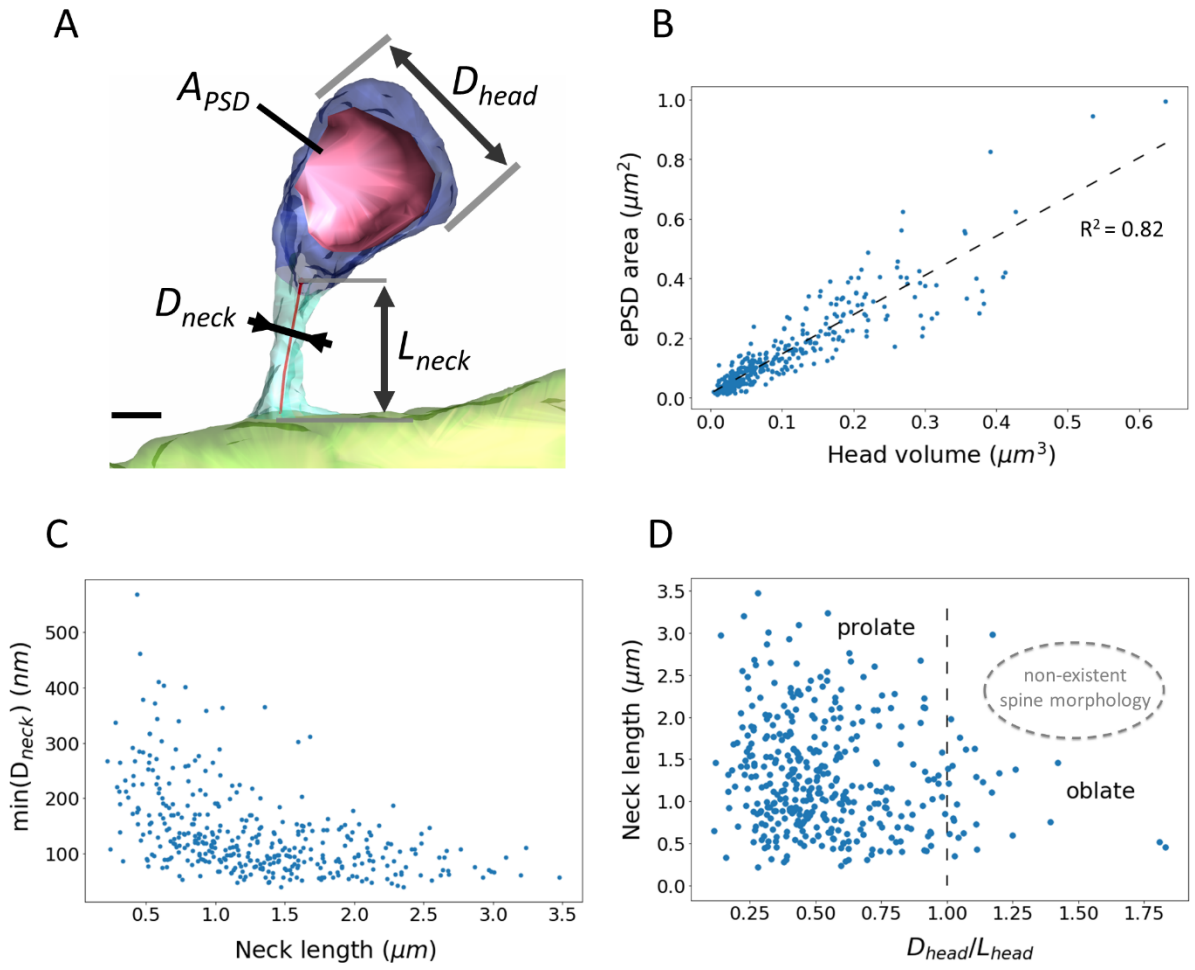

Figure 2. Spine morphometry along basal dendrites of layer 2/3 cortical pyramidal neurons.

(A) 3D-reconstruction of a dendritic spine from a SBEM stack. Dendritic shaft is in light green, spine neck in turquoise, spine head in blue and PSD surface in red. The following parameters were measured : PSD area, head diameter, neck diameter and neck length. Scale bar: 300 nm.

(B) Linear correlation of PSD area and spine head volume. R^2=0.82.

(C) Plot of the minimal spine neck diameter as a function of spine neck length. Spearman correlation coefficient is -0.58.

(D) Neck length as a function of spine head orientation, as quantified by the ratio of spine head diameter (D_{head}) over its length (L_{head}). $D_{head}/L_{head} < 1$ corresponds to a prolate spine head, which shape is stretched longitudinally with respect to the neck. $D_{head}/L_{head} > 1$ characterizes an oblate spine head, oriented orthogonally to the neck. The dashed line corresponds to $D_{head}/L_{head} = 1$. We did not observe any oblate spine with a long neck (non-existent spine morphology).

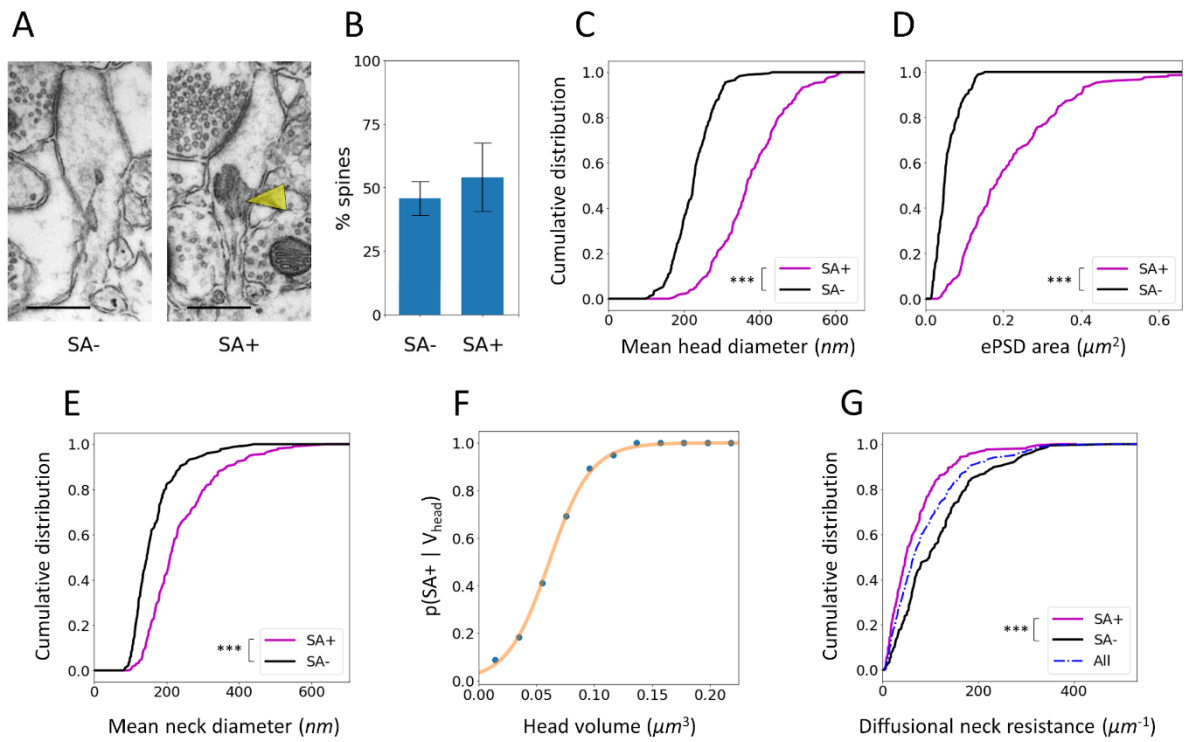

Figure 3. Ultrastructural comparison of spines with and without a spine apparatus.

(A) TEM images of spines either devoid of spine apparatus (SA-, left) or containing a spine apparatus (SA+, right, yellow arrowhead). Scale bars: 500nm.

(B) Proportion of SA- and SA+ spines. Histogram represents mean ± SD (N=390 spines).

(C) Distribution of mean head diameter for SA- and SA+ spines. N=179 and 221, respectively ($p < 10^{-38}$).

(D) Distribution of ePSD area. ($p < 10^{-40}$)

(E) Distribution of mean neck diameter. ($p < 10^{-12}$)

(F) Probability of harboring a SA as a function of spine head volume. Blue: experimental data. Orange: sigmoid fit.

(G) Distribution of the diffusional resistance of the spine neck (W_{neck}) calculated based on neck morphology. ($p < 10^{-5}$).

***p<0.001 calculated using Mann-Whitney test.

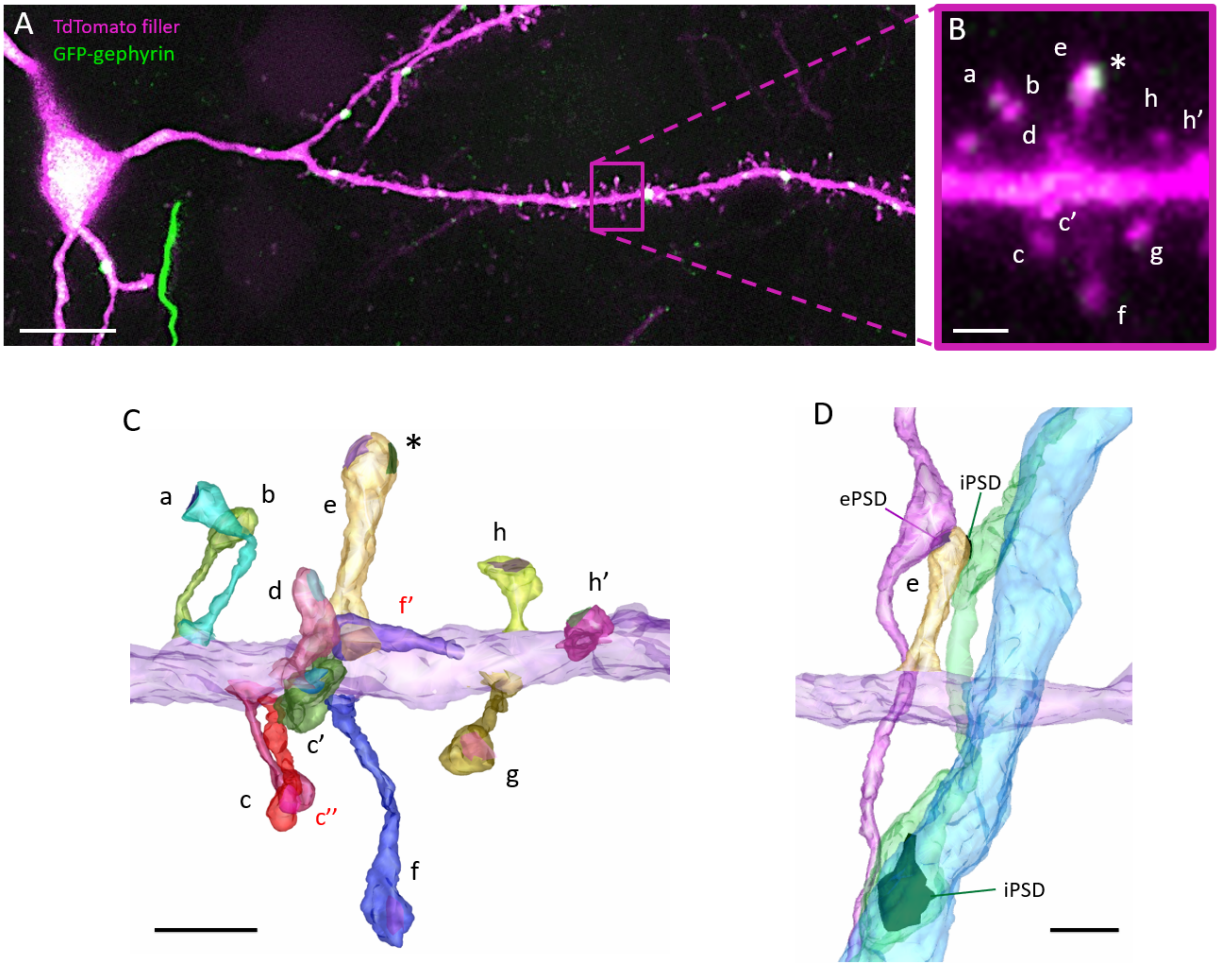

Figure 4. Identification of excitatory and inhibitory synapse on DiSs using CLEM.

(A) Confocal image of basal dendrites of a cortical L2/3 PN that was electroporated with cytosolic TdTomato and GFP-GPHN to label inhibitory synapses. The magenta rectangle outlines the region enlarged in B.

(B) Enlargement of a portion of the dendrite in A harboring several dendritic spine (lettered). Spine “e” contains a cluster of GFP-GPHN (asterisk) and corresponds to a putative dually-innervated spine (DiS).

(C) 3D-EM reconstruction of the same dendritic fragment as in B. Dendritic shaft is colored in purple; individual spines and PSDs are colored randomly. Spines visible in EM but not in LM are labelled in red. The inhibitory PSD (colored in green) on spine “e” is identified based on the position of the GFP-GPHN cluster (asterisk in B and C). GFP-GPHN-negative PSDs are defined as excitatory.

(D) 3D-EM reconstruction of spine "e" (yellow) with its presynaptic partners (magenta and green). As the “green” axon also targets a neighboring dendritic shaft (blue), it is defined as inhibitory. Scale bars: A: 10 µm; B, C, D: 1 µm.

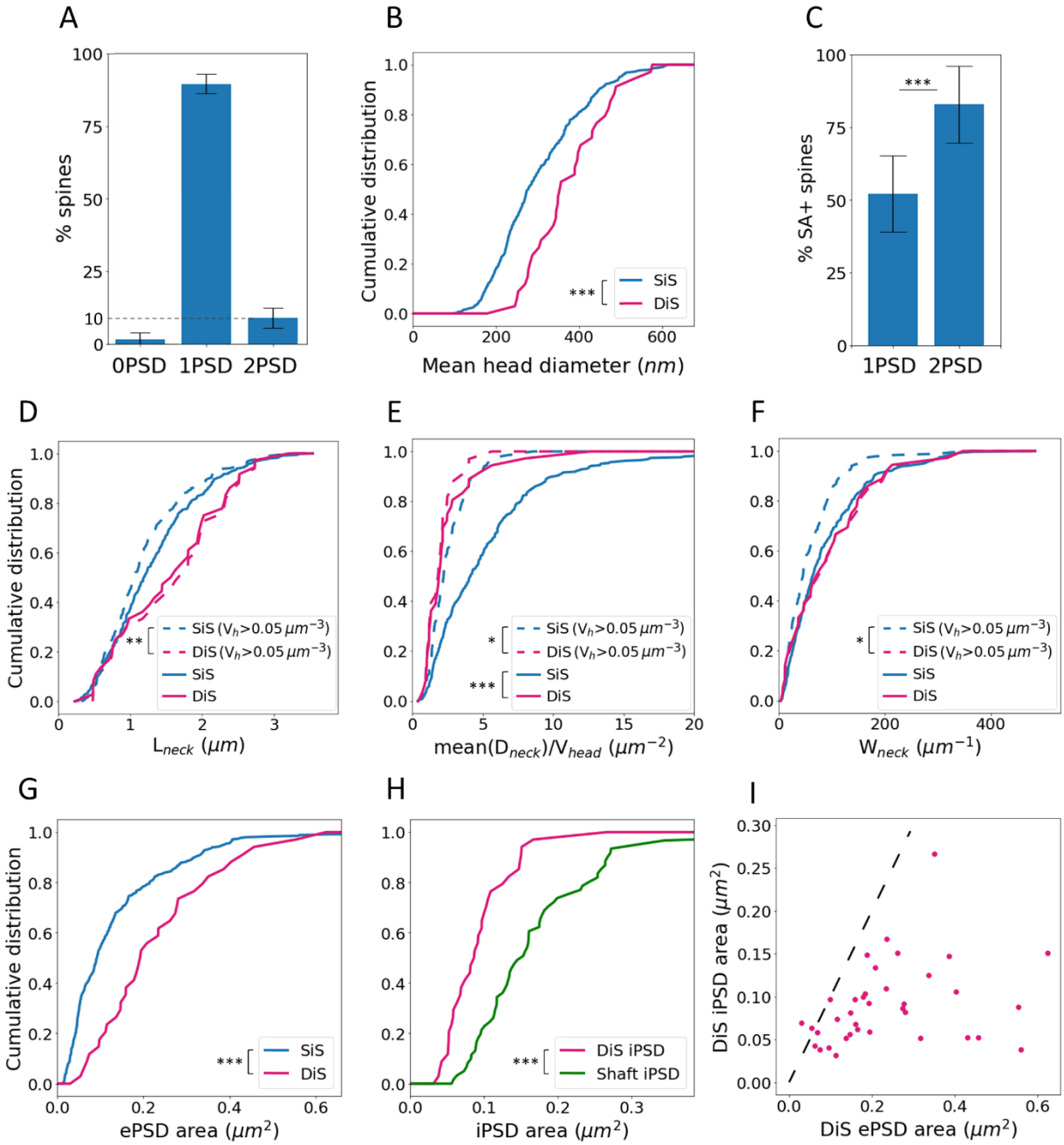

Figure 5. Anatomical properties of DiSs.

(A) Proportion of spines harboring 0, 1 or 2 synaptic contacts, quantified with CLEM. Histograms represent mean ± SD from, 390 spines in 8 dendrites.

(B) Quantification of mean spine head diameter for SiSs (blue) and DiSs (red). ($p < 10^{-4}$).

(C) Proportion of SiSs and DiSs harboring a SA. ($p < 10^{-10}$ using Pearson's χ^2 test)

(D-F) Quantification of neck length (D), the ratio between mean neck diameter and head volume (E) and the diffusional neck resistance (W_{neck}) (F) between SiSs and DiSs (solid lines,

N=349 and 37, respectively) and between DiSs with SiSs of similar head volume (spines with V_{head}>0.05 μm^3, dashed lines, N=186 and 34, respectively).

(G) Quantification of iPSD area in DiSs and dendritic shafts. N=37 and 62, respectively ($p < 10^{-6}$).

(H) Quantification of ePSD area in SiSs or DiSs. ($p < 10^{-5}$).

(I) Plot of iPSD area as a function of ePSD area in individual DiSs. The dashed line (y = x) highlights that the ePSD is larger than the iPSD in most of DiSs. N=37.

p-values were computed using Mann-Whitney test (B, D-H) or Pearson's χ^2 test (C). Only significant (p<0.05) p-values are shown (*p<0.05; **p<0.01; ***p<0.001).

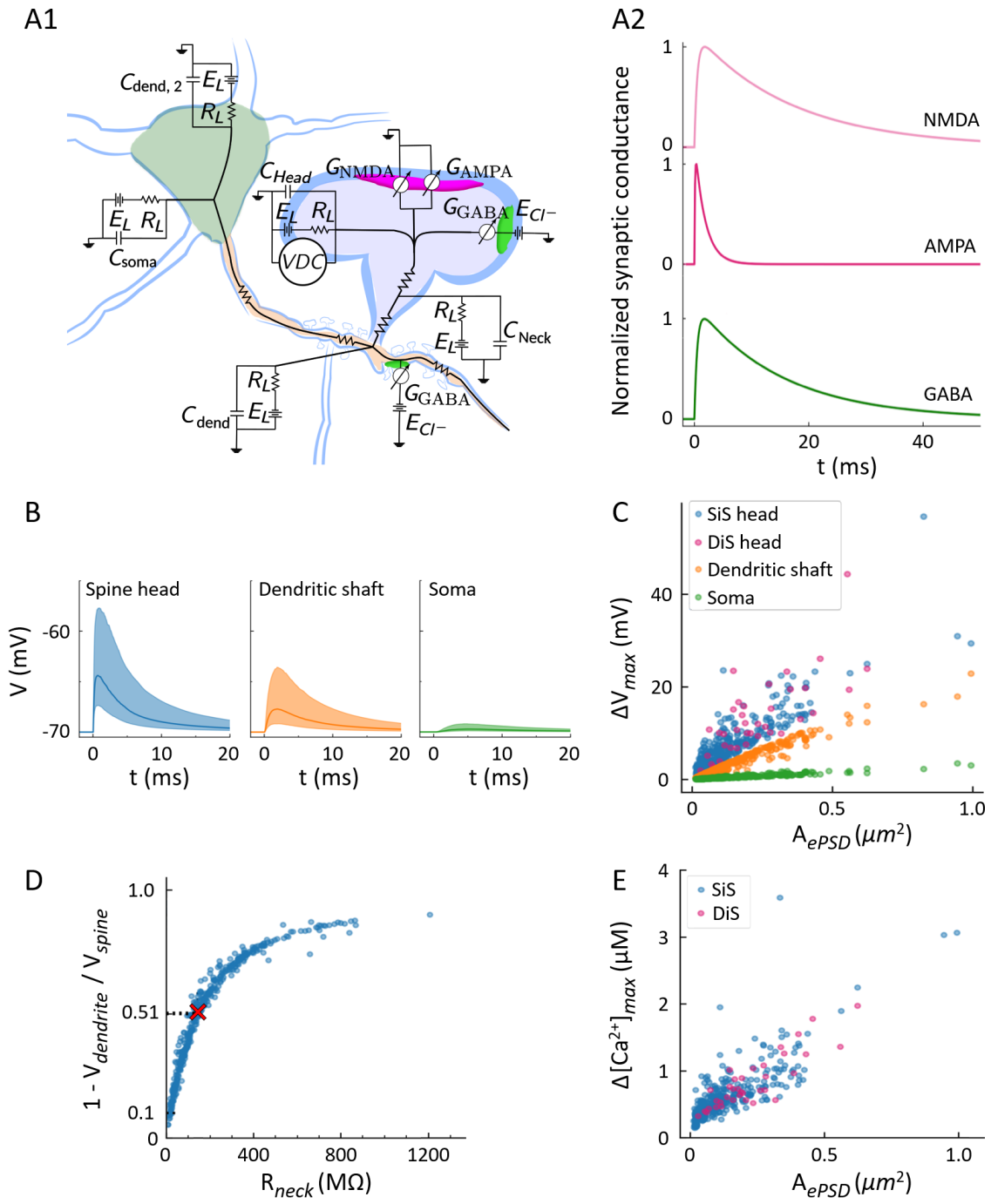

Figure 6. Morphologically-constrained model of synaptic signaling.

(A) Schematic of the circuit model (A1) and representative time-course of excitatory (magenta) and inhibitory (green) conductance based on the kinetics of AMPA, NMDA and $GABA_A$ receptors (A2). All compartments include passive resistor-capacitor circuits to model cell membrane properties and optionally include an active conductance that models voltage-dependent currents (VDC). All modeled spines feature an excitatory synapse with glutamatergic AMPA and NMDA currents. Spines and dendritic compartments can also

feature an inhibitory synapse with GABAergic currents. All conductances were scaled to PSD area (see Methods).

(B) Simulation of the time-courses of membrane depolarization following an EPSP, taking into account spine diversity (i.e. R_{neck}, ePSD area and distance to soma, as measured in CLEM). Membrane voltage is monitored over time in the spine head (blue), in the dendritic shaft in front of the spine (orange) and in the soma (green). Median voltage transients are plotted as solid lines. Shaded areas represent 68% confidence intervals, which span approximately one standard deviation on each side of the mean.

(C) Amplitude of evoked depolarization (ΔV_{max}) as a function of ePSD area at three distinct locations: head of SiSs (blue) or DiSs (magenta) where the EPSP was elicited, dendritic shaft 1 µm from the spine (orange) or soma (green).

(D) Attenuation of the amplitude of depolarization between the spine head and the dendrite as a function of the resistance of the neck (R_{neck}). The attenuation was calculated as: $\alpha = 1 - \Delta V_{max,\ shaft}/\Delta V_{max,\ spine}$. Red cross: mean value of α.

(E) Estimated amplitude of intracellular calcium concentration transients $\Delta[Ca^{2+}]_{max}$, following activation of NMDA receptors and VDCCs as a function of ePSD area. Three spiking outliers are not represented.

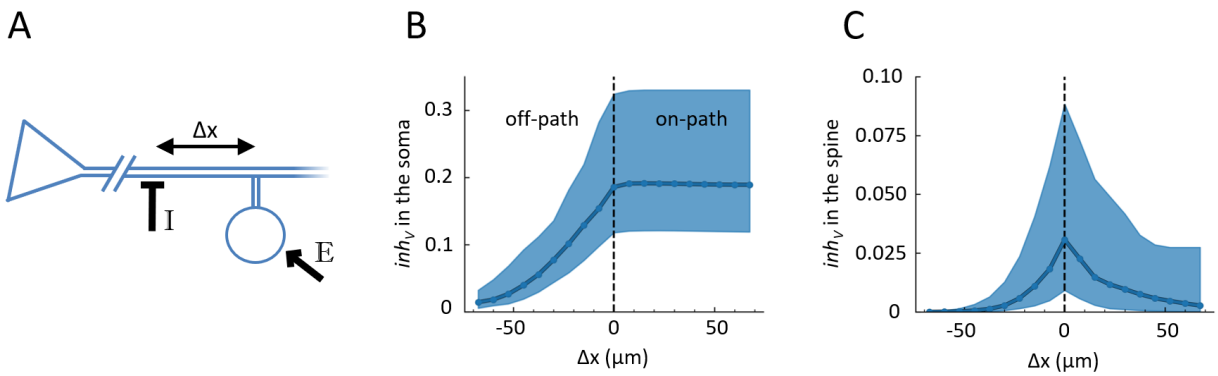

Figure 7. Effect of the distance between excitatory and inhibitory synapses on the integration of coincident EPSPs and IPSPs.

(A) Sketch: an EPSP was elicited in the spine and an IPSP in the shaft at a distance Δx from the spine.

(B-C) Voltage inhibition, inh_V, calculated in the soma (B) or in the spine head (C) as a function of Δx, for N=3700 iterations of the model. On-path inhibition: Δx > 0; off-path inhibition: Δx < 0. Solid lines represent medians. Shaded areas represent 68% confidence intervals, which span approximately one standard deviation on each side of the mean.

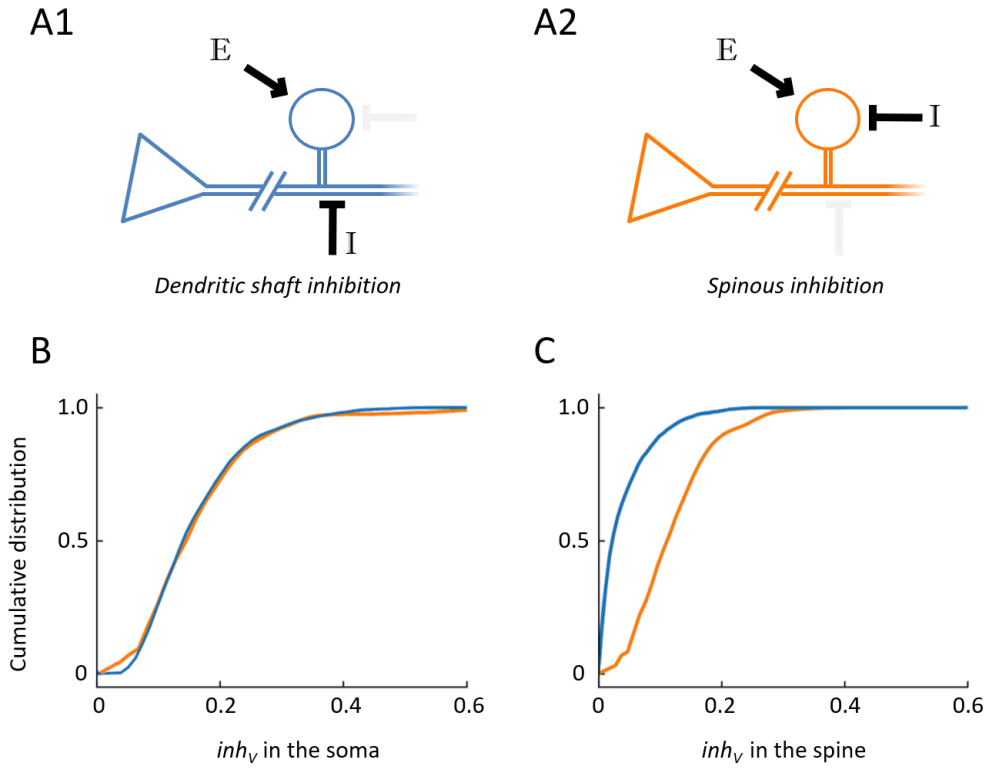

Figure 8. Effect of dendritic and spinous inhibition on EPSPs.

(A) Sketches: an EPSP (arrow) was elicited in a bootstrapped DiS placed randomly along the dendrite, and an IPSP (┬ symbol) was elicited either in the dendritic shaft at Δx = 0.7 µm from the stem of the spine (A1, blue) or directly in the spine head (A2, orange).

(B-C) Quantification of the inhibitory impact, inh_V, in the soma (B) and in the spine head (C) for N=3700 iterations of the model. Blue: dendritic inhibition; Orange: spinous inhibition.

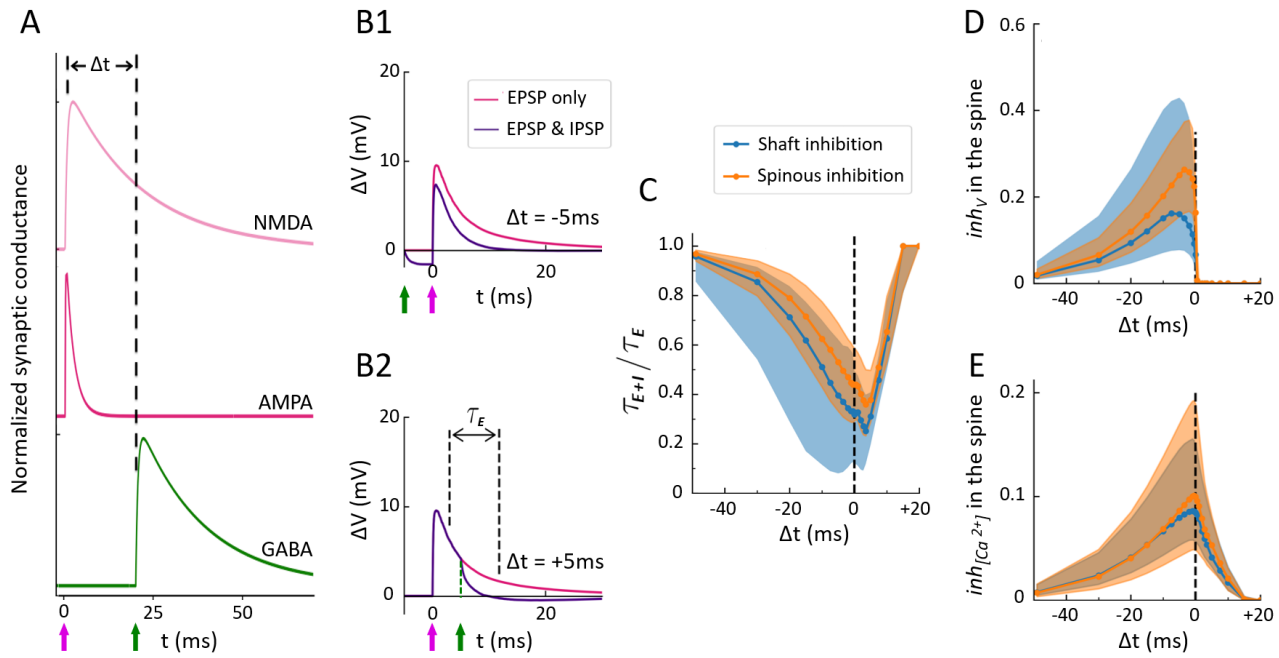

Figure 9. Effect of input timing on EPSP and IPSP integration.

(A) Schematic: excitatory AMPA and NMDA conductances were activated at t=0. The inhibitory GABAergic conductance was activated at an interval Δt before or after the onset of excitation.

(B) Examples of the time-course of depolarization in the spine head for Δt = +5 ms (B1) and Δt = -5 ms (B2) (purple curves) compared to no inhibition (magenta curves) for E_{Cl^-} = -80 mV and V_{rest} = -70 mV. Arrows represent the onset of excitatory and inhibitory inputs (magenta and green arrows, respectively). τ_E represents the 80-to-20% decay time (case with no inhibition).

(C) Ratio of 80-to-20% decay time of membrane depolarizations in the presence of inhibition (τ_{E+I}) over that without inhibition (τ_E) as a function of Δt for dendritic (blue) or spinous (orange) inhibition. Solid lines represent medians. Shaded areas represent 68% confidence intervals, which span approximately one standard deviation on each side of the mean.

(D) Voltage inhibition in the spine head, inh_V, induced by dendritic (blue) or spinous (orange) IPSPs as a function of Δt.

(E) Inhibition of the calcium influx in the spine head, $inh_{[Ca^{2+}]}$, induced by dendritic (blue) or spinous (orange) IPSPs as a function of Δt.